Protease-Activatable Porphyrin Molecular Beacon for Osteoarthritis Management

Connor Walsh,[#] Maneesha A. Rajora,[#] Lili Ding, Sayaka Nakamura, Helal Endisha, Jason Rockel, Juan Chen,* Mohit Kapoor,* and Gang Zheng*

Cite This: *Chem. Biomed. Imaging* 2023, 1, 66−80

Read Online

ACCESS | Metrics & More | Article Recommendations | Supporting Information

ABSTRACT: Despite the substantial burden posed by osteoarthritis (OA) globally, difficult challenges remain in achieving early OA diagnosis and adopting effective disease-modifying treatments. In this study, we use a biomolecular approach to address these limitations by creating an inherently theranostic molecular beacon whose imaging and therapeutic capabilities are activated by early pathological changes in OA. This platform comprised (1) a peptide linker substrate for metalloproteinase-13 (MMP-13), a pathological protease upregulated in OA, which was conjugated to (2) a porphyrin moiety with inherent multimodal imaging, photodynamic therapy, and drug delivery capabilities, and (3) a quencher that silences the porphyrin's endogenous fluorescence and photo-reactivity when the beacon is intact. In diseased OA tissue with upregulated MMP-13 expression, this porphyrin molecular beacon ($PP_{MMP13}B$) was expected to undergo sequence-specific cleavage, yielding porphyrin fragments with restored fluorescence and photoreactivity that could, respectively, be used as a readout of MMP-13 activity within the joint for early OA imaging and disease-targeted photodynamic therapy. This study focused on the synthesis and characterization of $PP_{MMP13}B$, followed by a proof-of-concept evaluation of its OA imaging and drug delivery potential. In solution, $PP_{MMP13}B$ demonstrated 90% photoactivity quenching in its intact form and robust MMP-13 activation, yielding a 13-fold increase in fluorescence post-cleavage. In vitro, $PP_{MMP13}B$ was readily uptaken and activated in an MMP-13 cell expression-dependent manner in primary OA synoviocytes without exuding significant cytotoxicity. This translated into effective intra-articular cartilage (to a 50 μm depth) and synovial uptake and activation of $PP_{MMP13}B$ in a destabilization of the medial meniscus OA mouse model, yielding strong fluorescence contrast (7-fold higher signal than background) at the diseased joint site. These results provide the foundation for further exploration of porphyrin molecular beacons for image-guided OA disease stratification, effective articular delivery of disease-modify agents, and OA photodynamic therapy.

KEYWORDS: *Molecular Beacon, Porphyrin, Osteoarthritis, Photodynamic Therapy, Molecular Imaging, Fluorescence, Drug Delivery*
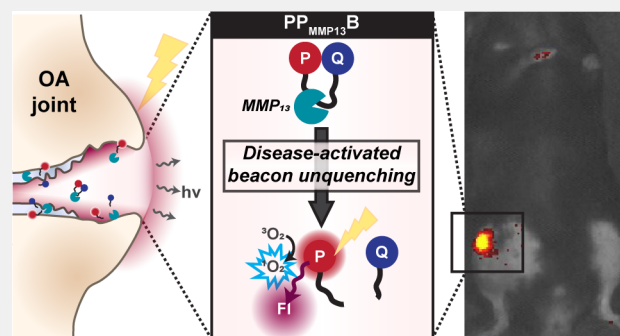
1. INTRODUCTION

Osteoarthritis (OA) is a debilitating degenerative joint disease that affected over half a billion patients globally in 2019 alone.[1] Its symptoms characteristically include joint stiffness, joint tenderness, pain and joint dysfunction that can yield disability and substantially decrease patient quality of life.[2] In the face of wide-reaching impacts of OA and projections for increasing prevalence over the next decade,[3] more impactful management strategies are needed for disease diagnosis, therapy and monitoring disease progression. Conventionally, OA diagnoses are reached by pairing clinical symptoms with radiographic findings (joint narrowing, osteophytes (bone spurs), sclerosis).[4] However, radiography is limited to the visualization of bony structural changes and thus cannot adequately capture all joint tissue implicated in OA. Consequently, patient symptoms can often present in the absence of any OA radiographic findings, leading to later stage diagnoses.[4,5] Magnetic resonance imaging

(MRI) techniques have made visualization of earlier soft tissue structural damage feasible, but are more costly, less readily available and, like radiography, still rely on the presence of appreciable changes in tissue morphology for diagnosis.[5,6] Thus, clinically available imaging options cannot capture the early molecular pathophysiological stages of OA that precede such structural damage. As there are currently no disease-modifying treatments for OA, diagnostic techniques that can detect early stage OA are particularly important for secondary disease
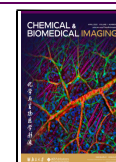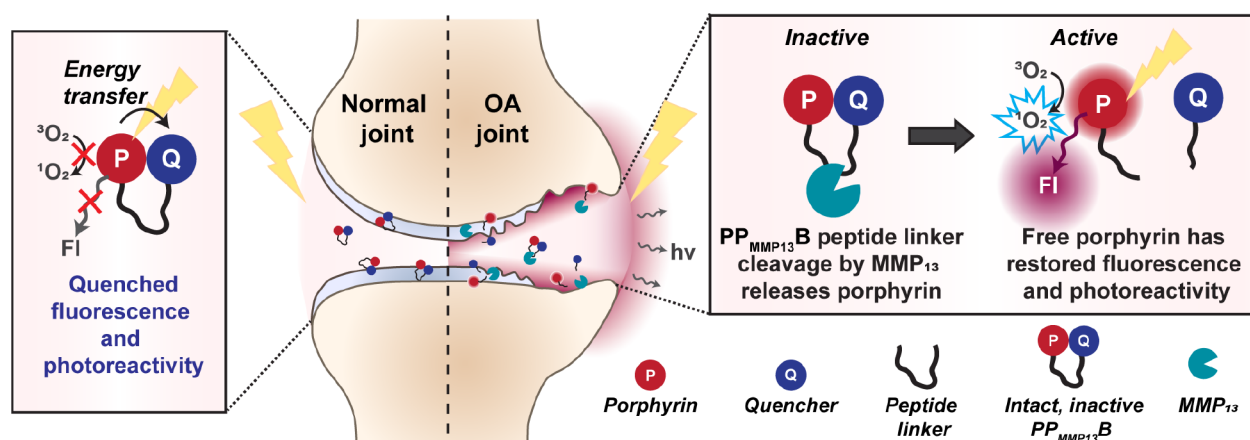
Figure 1. Illustration of the OA fluorescence imaging and therapeutic potential of $PP_{MMP13}B$. In a normal joint without substantial MMP-13 expression, the fluorescence and singlet oxygen generating capabilities of $PP_{MMP13}B$ would be quenched, rendering it theranostically inactive. In diseased environments with MMP-13 overexpression, $PP_{MMP13}B$ would be expected to undergo enzymatic cleavage, freeing the porphyrin from the BHQ3 quencher and restoring porphyrin photoactivity.

prevention, slowing disease progression, and improving patient outcomes.[7]

To this end, biomolecular approaches are gaining interest to overcome the limitations of structural OA imaging techniques and to enable OA-specific disease-modifying therapies. These approaches are built upon the understanding that OA is a disease of the entire joint, encompassing pathological changes to multiple tissues, including the muscle, articular cartilage, synovial membrane, and underlying subchondral bone.[8] In normal joints, cartilage is maintained by chondrocytes through a balance of anabolic and catabolic processes. These chondrocytes are nourished by synovial fluid produced by synovial fibroblasts within the synovial membrane, which also clears waste from the joint space through its vasculature and lymphatic vessels. Mechanical forces exerted upon the joint are effectively absorbed and dissipated by the cartilage, subchondral bone, and osteochondral junction. In OA, this delicate homeostasis is disturbed.[9,10] Changes to the kinematics experienced by cartilage alters joint loading, contributing to disease initiation.[11] Associated dysregulation of the chondrocyte microenvironment triggers increased breakdown of the cartilage extracellular matrix, disrupting the balance of anabolic and catabolic activities within the joint cartilage, contributing to OA progression.[10] This catabolic cartilage breakdown is caused by degradative proteases whose overproduction is stimulated by proinflammatory cytokines, namely IL-1β and TNF-α, among other biochemical stress factors.[12,13] The resulting cartilage fragments are released into the synovial fluid and subsequently interact with the nearby synovial membrane, resulting in synovial inflammation (synovitis).[14,15] Synovitis yields further proinflammatory cytokine release and catabolic protease production by both SFs and activated synovial macrophages, further stimulating catabolic activity.[16] The overall resulting degradation further destabilizes joint mechanics, leading to the bone remodeling visible on radiography.[17,18] This combined alteration of joint mechanics, chondrocyte catabolic activity and synovitis yield a vicious positive feedback loop of cartilage degradation and joint destruction.[16] At the heart of this process are catabolic proteases that are responsible for executing the cartilage degradation characteristic to OA. They could consequently be ideal biomolecular targets for novel OA diagnostics and therapy.

Of these catabolic proteases, matrix metalloproteinase-13 (MMP-13) is of particular interest as a biomarker and therapeutic target due to its key contributions to OA pathogenesis.[19] MMP-13 belongs to a class of zinc-dependent endopeptidases that digest extracellular matrix.[20] It is recognized as the primary MMP in OA responsible for articular collagen degradation, making it an ideal therapeutic and drug delivery target.[21−23] Its upregulated production in OA chondrocytes and synovium also makes MMP-13 a promising biomarker for OA diagnostics.[13,24,25] This potential is strengthened by clinical studies that demonstrating that increases in synovial MMP-13 levels correspond to increasing OA grade.[25,26] As such, the use of MMP-13 as an OA biomarker could open doorways to both earlier OA diagnosis and OA progression monitoring.

We leveraged these advantages to develop a new MMP-13-activatable porphyrin peptide molecular beacon ($PP_{MMP13}B$) rationally designed to encompass OA pathogenesis-driven imaging, therapy and drug delivery capabilities. The molecular beacon comprises three constituents (Figure 1): an MMP-13 cleavable peptide (GPLG−FRVGK) linking together porphyrin (pyropheophorbide-*a*) and a quencher (black hole quencher 3; BHQ3). When intact, the peptide constrains the porphyrin and BHQ3 moieties spatially, quenching the fluorescence and photoreactivity of the porphyrin through resonance energy transfer to BHQ3. However, in the presence of MMP-13, the peptide is cleaved, freeing the porphyrin from the BHQ3 quencher and restoring its photoactivity. Consequently, it would be expected that in environments with minimal MMP-13 production, such as in healthy joint tissue, $PP_{MMP13}B$ would not be largely fluorescent. Contrarily, in diseased joints with upregulated MMP-13 production, cleavage of $PP_{MMP13}B$ would be expected, yielding fluorescence at the joint site following light irradiation. This model of MMP-activated fluorescence has been previously validated and used to characterize disease progression in mouse models of OA with a commercial beacon.[27] However, $PP_{MMP13}B$ distinctly advances the utility of molecular beacons for OA diagnostics and therapy through two key design components.

First, our molecular beacon uses a modified peptide sequence link (GPLGFRVGK) based on previously identified peptide substrates with greater MMP-13 selectivity and catalytic activity.[28,29] Second, by using porphyrin, and specifically

pyropheophorbide-*a* (pyro), as our fluorophore, we unlock theranostic avenues unfeasible with conventional commercial beacons. Pyro is a near-infrared (NIR) fluorophore with a central macrocyclic ring that can be effectively chelated to metals.[30] This metal chelation allows pyro's imaging arsenal to extend beyond fluorescence to include positron emission tomography and MRI.[31,32] Pyro's macrocyclic structure also enables it to serve as a potent photosensitizer. When irradiated with NIR laser light, pyro generates singlet oxygen ($^1O_2$) through a type II photodynamic therapy (PDT) reaction.[33] This PDT effect has been shown in models of rheumatoid arthritis to selectively remove inflamed synovium, protecting joint cartilage from further damage.[34,35] Previous studies also demonstrated PDT to beneficially affect vertebral bone architecture, structural integrity, and mechanical stability.[36,37] PDT could thus play a role in breaking the cycle of cartilage degradation in OA by addressing synovitis and improving bone mechanical stability. The inclusion of pyro in $PP_{MMP13}B$ enables these therapeutic capabilities: In an intact state, the fluorescence and PDT abilities of pyro would be silenced, but in the presence of MMP-13 in a diseased OA joint, pyro fluorescence and $^1O_2$ generation would be restored for disease-targeted image-guided therapy. As an added advantage, pyro may overcome the continued challenge faced in the OA field of delivering drugs to the highly impermeable articular cartilage. Porphyrins and porphyrin-conjugates have been shown to intercalate in lipid membranes, readily undergo nonspecific cell uptake and facilitate the tissue retention of otherwise difficult-to-deliver agents.[38−41] Accordingly, we postulate this will translate into effective cellular uptake, articular deposition and tissue retention of the pyro−peptide conjugate, which could be leveraged to improve drug delivery to articular cartilage. Taken together, these multifaceted capabilities make $PP_{MMP13}B$ an intriguing activatable theranostic agent with multimodal imaging, PDT and drug delivery potential for pathogenesis-driven OA management. In this study, we focus on the synthesis, characterization, and validation of $PP_{MMP13}B$'s activatable fluorescence properties, followed by exploration of its drug delivery and fluorescence imaging potential in a mouse model of OA.

2. MATERIALS AND METHODS

2.1. General Materials

Fluorescence and UV−vis spectra were collected with a HORIBA FluoroMax-4 spectrofluorometer and Cary 60 UV−vis spectropho-tometer, respectively. Pyropheophorbide-*a* acid (pyro) was prepared according to literature.[42] Black hole quencher-3 carboxylic acid succinimidyl ester (BHQ3-NHS) was purchased from LGC Biosearch Technologies. Recombinant human MMP-13, ADAMTS-4, and ADAMTS-5 enzymes were purchased from R&D Systems (Minneapolis, MN). MMP Multipacks were purchased from Enzo Life Sciences. Proteinase K and singlet oxygen sensor green (SOSG) were purchased from Thermo Scientific and Invitrogen, respectively. Peptides on solid support resin were purchased from GL Biochem (Shanghai) Ltd. MMP buffer comprised 50 mM HEPES, 10 mM CaCl$_2$, and 0.05% Brij 35, pH 7.5. ADAMTS buffer contained 50 mM Tris, 100 mM NaCl, 5 mM CaC$_2$, and 0.05% Brij 35, pH 7.5. All other reagents were purchased from Sigma (St. Louis, MO).

2.2. Liquid Chromatography Methods

Reverse-phase preparative HPLC was performed on an Agilent ZORBAX 300SB-C18 column (300 Å, 5 μm, 9.4 × 250 mm) using a Waters 600 controller with a 2487 dual wavelength absorbance detector (Waters Canada, Ontario, Canada). The HPLC conditions were as follows: solvent A = 0.1% trifluoroacetic acid (TFA); solvent B = acetonitrile (ACN); gradient, from 70% A and 30% B to 100% B in 35

min, 100% B for 5 min, then to 70% A and 30% B for 10 min; flow rate 5 mL·min^{-1}.

Reverse-phase uPLC-MS was performed on a Waters Acquity UPLC CSH phenyl-hexyl column (130 Å, 1.7 μm, 2.1 × 50 mm) with a Waters 2695 controller, a 2996 photodiode array detector, and a Waters triple quadrupole (TQ) mass detector (Waters Canada, Ontario, Canada). The uPLC conditions were as follows: solvent A = 0.1% TFA; solvent B = ACN; gradient, from 80% A and 20% B to 100% B in 4 min, 100% B for 2 min, then to 80% A and 20% B in 0.5 min and for an additional 1.5 min; flow rate 0.4 mL·min^{-1}.

2.3. Synthesis of Pyro-GPLGFR(pbf)VGK(boc)-Rink Amide Resin

Fifty milligrams of GPLGFR(pbf)VGK(boc) on solid support Rink amide resin with N-terminus fluorenylmethyloxycarbonyl (Fmoc) modification was purchased from GL Biochem (Shanghai) Ltd. To remove the Fmoc protecting group the peptide resin was incubated with 20% piperidine solution in dimethylforamide (DMF). After complete Fmoc removal, which was confirmed and quantified by UV−vis measurements of the reaction solution ($\varepsilon_{300\ nm}$= 7.87 × 10^3 M^{-1} cm^{-1}), the resin was washed with DMF. Pyropheophorbide-*a* acid (pyro) was added to the deprotected peptide to couple with the N-terminal glycine in the presence of *O*-(benzotriazol-1-yl)-*N,N,N′,N′*-tetramethyluronium hexafluorophosphate (HBTU) and *N,N*-diisopro-pylethylamine (DIPEA) (pyro/HBTU/peptide = 2:2:1; DIPEA = 2.5%). The reaction was mixed under argon overnight. The resulting product was washed with DMF and methanol (MeOH) and dried using a vacuum centrifuge.

2.4. Synthesis of Pyro-GPLGFRVGK(ε-NH$_2$) (PP$_{MMP13}$)

To cleave pyro−peptide from the solid support and deprotect the arginine and lysine side chains, pyro−peptide resin was incubated with a solution comprising 95% TFA, 2.5% water, and 2.5% TIS for 2 h. Sold resin was removed by filtration. The resulting solution was concentrated, and product was precipitated in anhydrous diethyl ether and dried to give PP$_{MMP13}$ (*m/z* calcd for C$_{76}$H$_{104}$N$_{18}$O$_{11}$ [M]$^+$ 1444.81, *m/z* found 1446.6 [M + H]$^+$, 723.9 [M + 2H]$^{2+}$, 483.1 [M + 3H]$^{3+}$). Some PP$_{MMP13}$ was kept and used for experimental controls.

2.5. Synthesis of Pyro-GPLGFRVGK-BHQ3 (PP$_{MMP13}$B)

The remaining PP$_{MMP13}$ was dissolved in anhydrous dimethyl sulfoxide (DMSO) and quantified by UV−vis ($\varepsilon_{410\ nm,\ MeOH}$ = 9.7 × 10^4 M^{-1} cm^{-1}). BHQ3-NHS was added at a 1.1× molar ratio under basic conditions (2.5% DIPEA), and the reaction was conducted for 3 h. The reaction progress was monitored by uPLC-MS until 95% product conversion was achieved, upon which point the reaction was ceased by precipitating the reaction mixture in anhydrous diethyl ether. The final product PP$_{MMP13}$B was dried by vacuum centrifugation before purification by preparative HPLC as described above. The purified final product was characterized by UV−vis and electrospray ionization (ESI) mass spectrometry (*m/z* calcd for C$_{109}$H$_{137}$N$_{24}$O$_{12}$ [M]$^+$ 1975.09, *m/z* found 988.1 [M + 2H]$^{2+}$), 659.3 [M + 3H]$^{3+}$), 494.4 [M + 4H]$^{4+}$).

2.6. Synthesis of Pyro-glgfrvgk-BHQ3 (DPP$_{MMP13}$B)

The D-amino acid sequence of GLGFRVGK was also purchased from GL Biochem (Shanghai) Ltd. The procedure described above for pyro and BHQ3 conjugation yielding PP$_{MMP13}$B was followed but using the D-peptide sequence to synthesize DPP$_{MMP13}$B (*m/z* calcd for C$_{109}$H$_{137}$N$_{24}$O$_{12}$ [M]$^+$ 1975.09, *m/z* found 659.0 [M + 3H]$^{3+}$). It was used as a noncleavable, negative experimental control that provided information on background nonspecific cleavage and fluorescence unquenching.

2.7. Quenching Efficiency Measurements

PP$_{MMP13}$ or PP$_{MMP13}$B (1 nmol) was dissolved in 1 mL of DMSO to a concentration of 1 μM. These solutions were diluted 1:100 in DMSO, and fluorescence spectra were collected on resulting working solutions on a HORIBA FluoroMax-4 spectrofluorometer (415/5 nm excitation, 650 to 750 nm emission collection). The quenching efficiency of PP$_{MMP13}$B was calculated from spectra area the curve using eq 1.

Quenching efficiency is expressed as average ± standard deviation of triplicate measurements.

$$\%QE = \left(\frac{AUC_{PP_{MM13}} - AUC_{PP_{MMP13}B}}{AUC_{PP_{MMP13}}} \right) \times 100\% \quad (1)$$

2.8. Measurement of Singlet Oxygen Generation

$PP_{MMP13}B$ or PP_{MMP13} (3 nmol) was dissolved in solution containing 2 μL of DMSO and 0.5 μL of Tween-80. These solutions were then diluted to 3 μM in 1 mL of MMP buffer (containing 50 mM HEPES, 10 mM CaCl$_2$, 0.05% Brij 35, pH 7.5). To obtain fully cleaved $PP_{MMP13}B$ samples, 2 μL of Proteinase K (20 mg·mL^{-1}) was added to the $PP_{MMP13}B$ solution, which was allowed to incubate for 2 h at 37 °C. Ten micrograms of SOSG was dissolved in 33 μL of methanol and diluted to 100 μM in PBS. SOSG and either PP_{MMP13}, intact $PP_{MMP13}B$, or cleaved $PP_{MMP13}B$ were added to a black 96-well plate with final concentrations of 10 μM and 0.5 μM respectively in a final volume of 200 μL. Wells containing only SOSG were used as controls. Light doses ranging from 0 to 25 J·cm^{-2} were delivered to each well using a 671 nm free-space laser (LaserGlow Technologies) at an irradiance of 50 mW·cm^{-2}. Fluorescence measurements were collected with a CLARIOStar microplate reader (BMG LABTECH) (SOSG settings: 490/8 nm excitation, 515−575 nm emission; pyro settings: 415/8 nm excitation, 650−700 nm emission). Intensities across the emission spectra wavelength range were integrated and normalized to SOSG controls. Singlet oxygen generation and PP_{MMP13} and $PP_{MMP13}B$ photobleaching were calculated by normalizing integrated fluorescence across emission wavelengths to the associated 0 J·cm^{-2} light-free control. Experiments were completed in triplicate and values are expressed as mean ± standard deviation.

2.9. MMP-13-triggered fluorescence activation of $PP_{MMP13}B$

$PP_{MMP13}B$ (1 nmol) was dissolved in a solution made of 5 μL DMSO and 0.5 μL Tween-80. This solution was then diluted into 500 μL MMP buffer. MMP-13 was activated by incubation with 1 mM amino-phenylmercuric acetate (APMA) for 1.5 h at 37 °C. The activated MMP-13 was added to the $PP_{MMP13}B$ solution at a 1:40 molar ratio. Activation was monitored by removing 5 μL sample aliquots at 0, 0.5, 1, 3, 6, 12, and 24 h. The aliquots were diluted 1:200 in MMP buffer before acquiring spectrofluorometer measurements (acquisitions as described above). Area under the curve was calculated and used to determine fold fluorescence increase over time relative to 0 h.

For kinetic activation studies, $PP_{MMP13}B$ was dissolved in a solution of 2 μL DMSO and 0.5 μL Tween-80. This solution was then added into 1 mL of MMP buffer. MMP-13 was activated by incubation with 1 mM APMA for 1.5 h at 37 °C. $PP_{MMP13}B$ was incubated alone or with MMP-13 at a 1:50 MMP-13:beacon molar ratio at 37 °C. Fluorescence was monitored in real time for 2 h at 1 min intervals using a ClarioStar plate reader (37 °C, 416 nm excitation, 674 nm emission).

2.10. Specificity toward various MMPs and ADAMTSs

$PP_{MMP13}B$ (1 nmol) was dissolved in a solution containing 2 μL DMSO and 0.5 μL Tween-80. This was then diluted into 100 μL MMP buffer. MMPs (MMP multipack-1 & −2, purchased from Enzo Life Science Inc.), ADAMTSs (ADAMTS-4 & −5, purchased from R&D Systems), or Proteinase-K was added. The reaction solution was incubated for 24 h at 37 °C. Following incubation, samples were diluted 1:1,000 in DMSO for fluorescence spectroscopy measurements to evaluate pyro fluorescence unquenching. Reaction solutions were diluted 1:1 in MeOH to stop enzymatic reactions and subsequently subjected to uPLC-MS analysis for detection of cleavage fragments. Select samples were processed using HiPPR Detergent Removal Spin Column Kit (Thermo Scientific) per manufacturer instructions prior to uPLC-MS. Experiments were completed in triplicate and values are expressed as mean ± standard deviation.

2.11. Patient information and cartilage samples

Human tissue collection and use were performed under REB #14−7592, "Longitudinal Evaluation in the Arthritis Program (LEAP) Addendum: Biomarker Exploration Analysis" at the Schroeder Arthritis

Institute, Krembil Discovery Tower, University Health Network. Informed consent was appropriately obtained and no unexpected safety hazards were encountered during patient tissue collection. Human OA cartilage and synovial tissue was obtained from consenting patients undergoing knee replacement (Kellgren-Lawrence grade III/IV: moderate to severe knee OA[43]) at the Schroeder Arthritis Institute (Toronto, ON). Human knee cartilage and synovium obtained from patients were immediately placed in Dulbecco's Minimum Essential Medium (DMEM; with 4.5 g·L^{-1} Glucose, with L-Glutamine & Sodium Pyruvate, Gibco) supplemented with 10% (v/v) fetal bovine serum (FBS) and 1% (v/v) penicillin/streptomycin (P/S) and subsequently stored at 4 °C.

2.12. Cell culture

Chondrocytes were extracted from the above cartilage samples by sequential enzymatic digestion.[44] Briefly, cartilage samples were washed with PBS supplemented with 5% P/S for 1 h at 37 °C. PBS was replaced with culture medium and the samples were left overnight at 37 °C in a humidified atmosphere of 5% CO$_2$/95% air. The following day, cartilage was incubated for 1 h with 0.1% (w/v) Pronase (Roche, #10165921001) in culture medium followed by 4 h with 0.2% (w/v) collagenase (Sigma, C0130) in culture medium. Enzyme solutions were passed through a 0.7 μm sterile syringe filter (Millex, Sigma) prior to use. Cells were cultured in 10 cm Petri dishes for 1−2 weeks in a humidified atmosphere of 5% CO$_2$/95% air until confluent. Medium was changed every 2−3 days. Confluent cultures were digested by 0.05% trypsin.

Fibroblast-like synoviocytes (SFs) were extracted from synovium samples by enzymatic digestion.[45] Briefly, Synovial membrane samples were washed with culture medium not containing FBS before incubating for 1 h at 37 °C with 0.1% (w/v) Trypsin (Sigma) in culture medium without FBS followed by 4 h with 0.2% collagenase type IA (w/v) (Sigma, C0130) in culture medium without FBS. Cells were cultured in 10 cm Petri dishes in a humidified atmosphere of 5% CO$_2$/95% air until confluent. Confluent cultures were passaged via 0.05% trypsin. Cells were used for experiments between the second and fifth passages.

Human umbilical vein endothelial cells (HUVECs) were kindly donated by Dr. Armand Keating (University of Toronto). Cells were cultured in 75 cm^2 cell culture flasks and maintained with Endothelial Cell Growth Base Media supplemented with Endothelial Cell Growth Supplement (R&D Systems, Minneapolis, MN). Medium was changed every 2−3 days. Confluent cultures were split/passaged with 0.25% trypsin.

2.13. Cytotoxicity assay

Toxicity of $PP_{MMP13}B$ toward human chondrocytes and SFs was determined using an alamarBlue assay. Cells were seeded at a density of 1×10^4 cells per well in 96 well plates (Greiner). After 24 h, medium was replaced, and beacon was added thereafter. Cells were treated with varying concentrations of $PP_{MMP13}B$: 7 nmol $PP_{MMP13}B$ was dissolved into a solution of 2 μL sterile DMSO and 0.5 μL Tween-80, which was then diluted into 350 μL sterile PBS to a final concentration of 20 μM. To each well, corresponding amounts of $PP_{MMP13}B$ solution were added to reach desired final test concentration (0, 0.1, 0.3, 0.5, 0.8, 1, 2, and 5 μM). After a 24 h treatment incubation period, cells were washed with PBS, which was then replaced with medium containing 0.5 mg·mL^{-1} alamarBlue (Invitrogen). Cells were incubated for 2 h, after which fluorescence emission was measured using a CLARIOStar microplate reader (BMG LABTECH) (540/15 nm excitation, 590/20 nm emission). Cell viability for each experiment was calculated by normalizing averaged blank-corrected fluorescence values of three replicate treatment wells to blank-corrected fluorescence values of wells treated with medium alone.

2.14. Flow cytometry

SFs or chondrocytes were seeded at 1×10^5 cells per well in a 6-well plate (Nunc). Cells were allowed to adhere for 24 h, after which media was replaced with 2 mL of fresh media. PP_{MMP13} (20 nmol) was dissolved into a solution of 5 μL of sterile DMSO and 1 μL of Tween-80. This solution was then diluted into 1 mL of sterile PBS to a final

concentration of 20 μM. This working solution was added to the wells for a final concentration of 1 μM PP$_{MMP13}$. The cells were allowed to incubate for another 1, 6, or 24 h, at which point the treatment medium was removed. Cells were washed with PBS before digestion with 0.25% trypsin. Cell suspensions were transferred to 15 mL centrifuge tubes and centrifuged at 180g for 5 min. The supernatant was removed, and the pellet was resuspended in PBS. Rinsing was repeated twice before cells were resuspended for a final time in PBS supplemented with 1% FBS before passing through a 35 μm nylon mesh cell strainer into polystyrene test tubes. Flow cytometry was conducted with an Accuri C6 (BD Biosciences) flow cytometer, using an APC filter (640 nm excitation, 675/25 nm emission) to assess pyro fluorescence. Histograms were generated and analyzed using FlowJo software. Experiments were completed in triplicate and results are presented as mean $\pm$ standard deviation.

2.15. Western Blots

Cells were seeded at 1.5×10^5 cells per well in 6-well plates. After 24 h of incubation, medium was changed. Chondrocytes were treated with 10 ng·mL^{-1} IL-1β and transforming growth factor beta (TGF-β) for 24 h. PP$_{MMP13}$ or PP$_{MMP13}$B (6 nmol) was dissolved into a solution of 6 μL of sterile DMSO and 0.75 μL of Tween-80. This solution was then diluted into 300 μL of sterile PBS to a final concentration of 20 μM. This treatment solution was added to the wells for a final concentration of 1 μM PP$_{MMP13}$ or PP$_{MMP13}$B. Cells were cultured for an additional 24 h. Upon termination of treatments, culture supernatant was collected and stored at -80 °C. Wells were washed with PBS before whole proteins were isolated with radioimmunoprecipitation (RIPA) buffer. Protein concentrations was measured by Bradford assay. Briefly, 5 μL of RIPA lysate (1:10 dilution in PBS) was incubated in the dark with 250 μL of Bradford reagent (Sigma) for 30 min in a 96-well plate, immediately after which absorbance at 595 nm was measured on a CLARIOStar microplate reader (BMG LABTECH). A standard curve was prepared by performing a serial dilution of bovine serum albumin (BSA). The BSA standard curve and all samples measurements were conducted in duplicate. Based on these measurements, protein solutions (20 μg protein total) were loaded into 10% SDS-polyacrylamide gels for electrophoresis at 137 V for approximately 1 h at RT. Separated protein was electroblotted onto polyvinylidene fluoride membranes at 100 V for 1 h at 4 °C. Membranes were blocked for 30 min with 10 mM Tris-buffered saline (TBS) containing 5% skim milk and probed for 1.5 h with rabbit polyclonal IgG primary antibodies (1:500) specific for MMP-13 (Abcam, catalog 39012), mouse polyclonal IgG primary antibodies (1:500) specific to α-SMA (Sigma, catalog A2547), or mouse monoclonal IgG (1:1,000) for β-actin (Sigma, catalog A1978) in blocking buffer. After washing the membrane three times with TBS containing 0.1% Tween-20 (TBST), the membrane was incubated overnight at 4 °C with HRP-conjugated antirabbit (Sigma, catalog SAB3700843) or antimouse (Sigma, catalog A2179) secondary antibodies (1:10,000) in TBS containing 5% skim milk. Membranes were subsequently washed in TBST. Protein bands were visualized with an enhanced chemiluminescence substrate (Clarify Western ECL Substrate, BIO-RAD and SuperSignal West Pico, Thermo Science) using a BIO-RAD Chemidoc apparatus. Blots were scanned and signal intensity was quantified using ImageJ (National Institutes of Health, USA).

2.16. Fluorescence Microscopy

SFs and HUVECs were cultured as described above. First, 5×10^3 cells were seeded per well in Nunc Lab-TekII-CC2 8-chambered slides. After 24 h, the medium was changed and to it was added PP$_{MMP13}$B, PP$_{MMP13}$, or DPP$_{MMP13}$B to a final concentration of 2.5 μM. The cells were incubated for an additional 24 h. Wells were washed with PBS, and cells were subsequently fixed with 500 μL of 4% paraformaldehyde in PBS for 20 min, after which the fixed cells were washed with PBS twice. The chamber was then removed, and 10 μL of mounting solution with 4′,6-diamidino-2-phenylindole (DAPI) (Vector Laboratories Inc.) was added to each well. The cells were covered by a cover slide and subjected to microscopic studies using an Olympus 1X73 inverted microscope (pyro: Cy5 620/60 nm excitation, 665 nm long-pass emission, nuclei: DAPI 375/28 nm excitation, 460/50 nm emission).

2.17. PP$_{MMP13}$B Cleavage in Cells by uPLC-MS Analysis

SFs and HUVECs were seeded in a 12-well plate (COSTAR) at 5×10^4 cells per well. After 2 days of incubation, media was changed and PP$_{MMP13}$B or DPP$_{MMP13}$B was added to the wells at a final pyro concentration of 20 μM. Cells were then allowed to incubate for 24 h, after which the cell supernatant was collected. Wells were washed with PBS, and cells were lysed with 50 μL RIPA buffer. Samples were dried completely by vacuum centrifugation. The dried samples were then redissolved in 100 μL DMSO and centrifuged for 5 min at 10,000 rpm (Eppendorf SE centrifuge) to remove any precipitate. The supernatant was filtered through a 0.45 μm cellulose acetate 4 mm syringe filter (National Scientific) and subjected to uPLC-MS.

2.18. In Vivo Animal Study in DMM Mouse Model

All in vivo animal experiments were approved by the University Health Network Animal Care Committee. Experiments adhered to all relevant institutional, provincial, and federal requirements. C57BL/6J mice (Jackson Laboratories, USA) were bred and housed in a 21 $\pm$ 1 °C controlled room under a 12-h light-dark cycle. Animal access to food and water was ad libitum. Twelve-week-old C57BL/6J male mice were subjected to destabilization of the medial meniscus (DMM) surgery in the right knee as previously described.[46] DMM mice (n = 5 per group) were anesthetized with isoflurane gas (1−2% v/v isoflurane, 1 L·min^{-1} flow rate, in 100% oxygen). The hindlimbs were epilated to allow for in vivo fluorescence imaging. Pretreatment whole-body in vivo fluorescence imaging scans were conducted under 1−2% v/v isoflurane anesthesia using a PerkinElmer Xenogen IVIS Spectrum Imaging System (level high, 675 nm excitation, 720 nm emission, epi-illumination, bin (HR) 4, FOV 22.3, f8 serial imaging with multiple exposures (0.5 to 7 s)) in a supine position. Mice were then administered 2 μL of 500 μM PBS solutions of PP$_{MMP13}$, PP$_{MMP13}$B, or DPP$_{MMP13}$B via intra-articular injection through a Hamilton syringe into the right knee, while 2 μL of sterile PBS was injected into the left knee as a contralateral control. Mice were imaged again directly after injection and then 6 h postinjection. After this last imaging time-point, animals were humanely euthanized by cervical dislocation under surgical plane isoflurane anesthesia. Knee joints and surrounding muscle tissue were excised, and ex vivo fluorescence imaging was performed with the same settings as above. Immediately following ex vivo fluorescence imaging, knee joints were processed for cryosectioning. Briefly, the joints were fixed in 4% paraformaldehyde in PBS for 12 h at 4 °C in tissue cassettes. After washing with PBS, joints were then decalcified for 7 days in 10% (w/v) ethylenediaminetetraacetic acid (EDTA; Sigma) in water. Cassettes were stirred in this EDTA solution at 4 °C in a beaker protected from light. EDTA solution was replaced after day 2 and day 5. After decalcification, cassettes were placed in a beaker of PBS and stirred to wash joints and then transferred to 30% (w/v) sucrose in water, stirred at 4 °C and protected from light overnight for joint cryopreservation. Joint cassettes were again washed with PBS before transferring joints to Eppendorf tubes. 80/20% OCT/PBS was added to each tube, and tubes were gently rocked for 2 h at 4 °C, followed by another 2 h in 100% OCT at 4 °C. Joints were then transferred to cryomolds, oriented such that the medial side of the joint was facing down in the cryomolds. OCT was added to the molds, and joints were snapped frozen over dry ice. The frozen blocks were stored at -80 °C until cryosectioning. Ten micrometer thick slices were cut using a cryostat and transferred to glass slides for fluorescence microscopy. To prepare slides for microscopy, slides were fixed in 10% formalin for 5 min and washed twice with PBS. Ten microliters of DAPI mounting solution was added to slides before covering with a cover slide and subjecting to microscopy using an Olympus 1X73 inverted microscope at 10× magnification (pyro: Cy5 channel 620/60 nm excitation, 665 nm long-pass emission, 750 ms exposure, DAPI: 375/28 nm excitation, 460/50 nm emission, 500 ms exposure).

2.19. Statistical Analysis

All statistical analyses were conducted in GraphPad Prism. One-way ANOVA tests were applied and Tukey's test was used use for posthoc analysis to evaluate statistically significant differences across multiple comparisons. All p values are presented in their corrected form for these
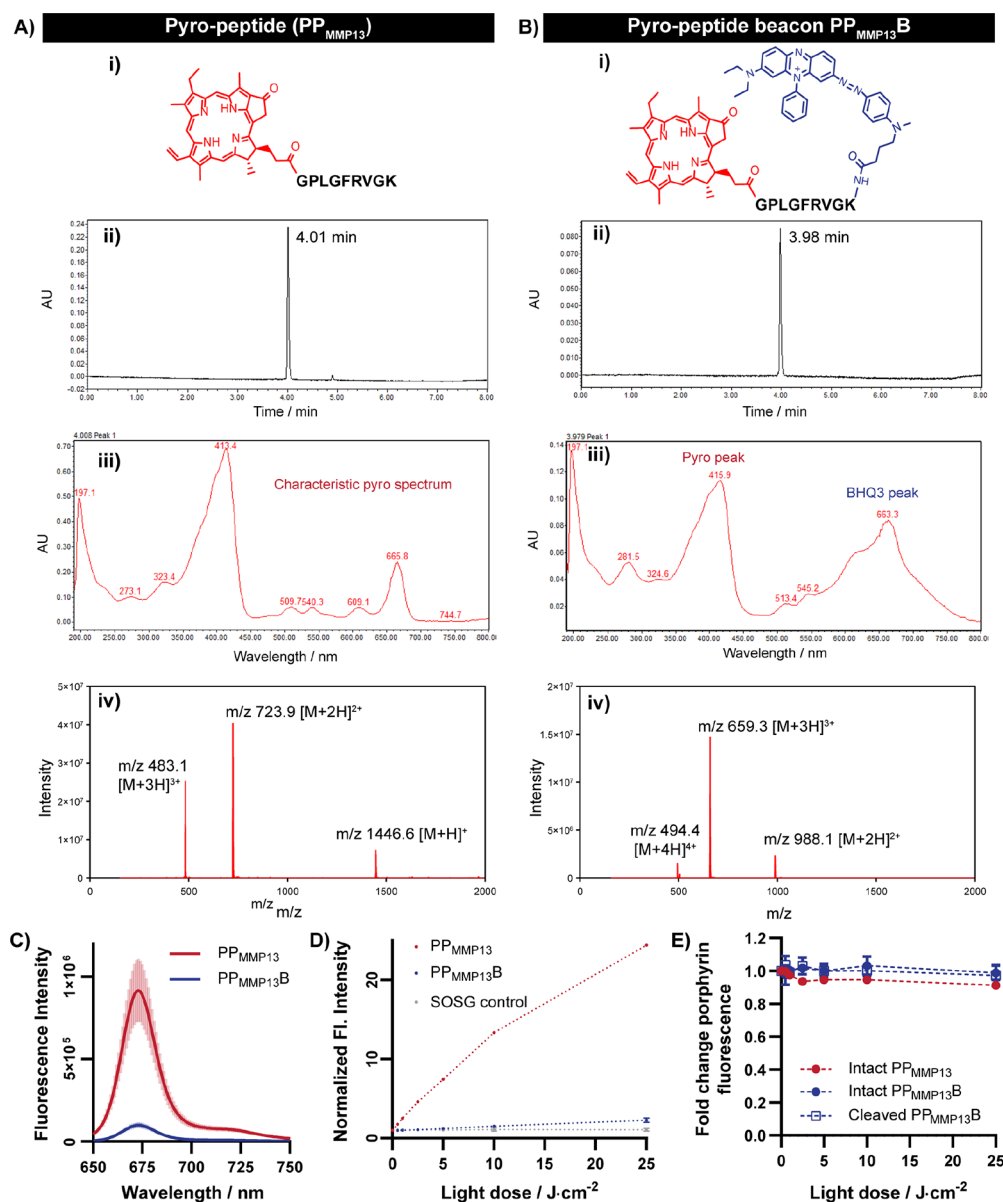
Figure 2. Characterization of PP_{MMP13} (A,i) and $PP_{MMP13}B$ (B,i) via uPLC-MS (A,B). The uPLC chromatographs (iii) of PP_{MMP13} and $PP_{MMP13}B$ show product with >98% purity. The associated UV−vis spectra (iii) yield characteristic pyropheophorbide a (pyro) peaks for both PP_{MMP13} and $PP_{MMP13}B$, with the latter also including the characteristic absorbance profile of BHQ3. This suggested effective conjugation of pyro to the MMP-13 peptide substrate and then subsequently also to BHQ3, which was confirmed by ESI-MS (iv). $PP_{MMP13}B$ fluorescence and singlet oxygen quenching were characterized by spectrofluorimetry (C) and a singlet oxygen sensor green (SOSG) assay (D) respectively, while (E) depicts the photostability of PP_{MMP13}, $PP_{MMP13}B$, and nonspecifically cleaved $PP_{MMP13}B$ fragments.

multiple comparisons. All replicates are presented as mean ± standard deviation.

3. RESULTS AND DISCUSSION

3.1. Synthesis of MMP13-Targeted Porphyrin Molecular Beacons

The synthesis of $PP_{MMP13}B$ is illustrated in Figure S1. Briefly, following Fmoc cleavage from the GPLGFRVGK peptide on solid support resin, pyro was coupled onto the N-terminal glycine residue, after which resin cleavage yielded PP_{MMP13}. This pyro−peptide in the absence of BHQ3 served as a positive perpetually "active" fluorescent and photoreactive positive control that also allowed for better assessment of pyro−peptide's drug delivery potential. Purification of PP_{MMP13} was

performed by prep-HPLC. This yielded PP_{MMP13} (Figure 2A) with 97% purity (as determined by uPLC), a characteristic pyro absorbance spectrum and expected ESI mass (m/z calcd for $C_{76}H_{104}N_{18}O_{11}$ $[M]^+$ 1444.81, m/z found 1446.6 $[M + H]^+$, 723.9 $[M + 2H]^{2+}$, 483.1 $[M + 3H]^{3+}$). To complete the synthesis of $PP_{MMP13}B$, BHQ3-NHS was then conjugated onto the amine of the C-terminal lysine side chain of PP_{MMP13} (Figure S1). Subsequent prep-HPLC purification yielded $PP_{MMP13}B$ with over 98% purity as determined by uPLC-MS, a distinct UV−vis spectrum containing both characteristic pyro (416 nm, broad) and BHQ3 (663 nm) peaks, and a concordant ESI MS mass signal (m/z calcd for $C_{109}H_{137}N_{24}O_{12}$ $[M]^+$ 1975.09, m/z found 988.1 $[M + 2H]^{2+}$), 659.3 $[M + 3H]^{3+}$), 494.4 $[M + 4H]^{4+}$) (Figure 2B). A negative control beacon for MMP-13 activation was also synthesized in the same manner but using D-
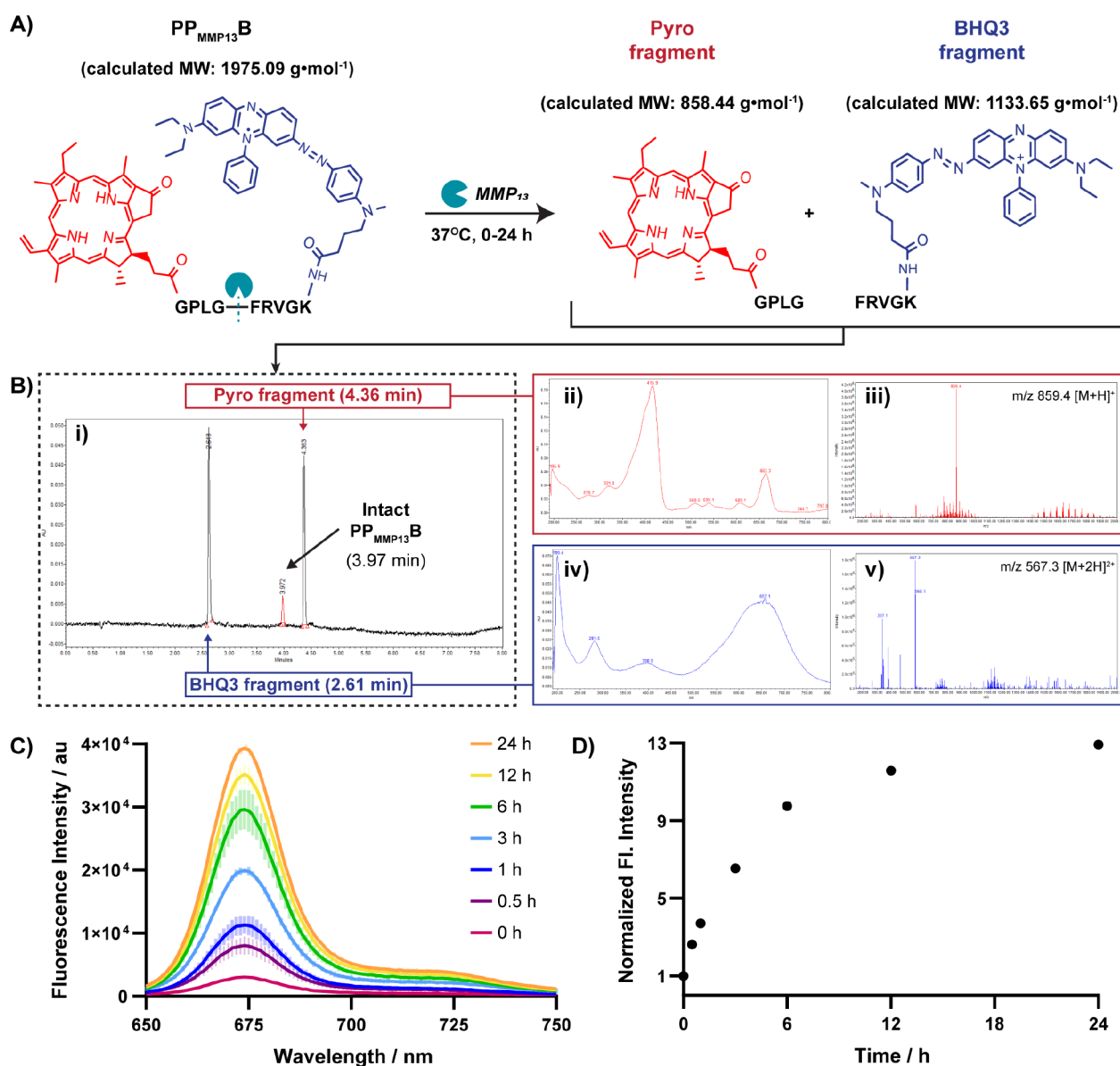
Figure 3. MMP-13-triggered cleavage and subsequent activation of $PP_{MMP13}B$. (A) Scheme of cleavage reaction and associated cleavage products. (B) Specific cleavage site was identified by characterizing the cleavage fragments by uPLC-MS. This $PP_{MMP13}B$ cleavage reaction unquenched the $PP_{MMP13}B$ fluorescence over time as assessed by spectrofluorimetry (C). Integration of fluorescence spectra demonstrated cleavage products generated approximately 13-fold higher fluorescence compared to intact $PP_{MMP13}B$ after 24 h (D).

amino acids to prevent site-specific proteolytic cleavage. This $DPP_{MMP13}B$ was similarly purified by prep-HPLC and characterized by uPLC to yield a product with over 97% purity, characteristic pyro and BHQ3 UV−vis peaks and confirmed identity via ESI MS (m/z calcd for $C_{109}H_{137}N_{24}O_{12}$ $[M]^+$ 1975.09, m/z found 659.0 $[M + 3H]^{3+}$) (Figure S2).

3.2. $PP_{MMP13}B$ Fluorescence and Singlet Oxygen Quenching

Fluorescence and $^1O_2$ generation from $PP_{MMP13}B$ were assessed in relation to PP_{MMP13} to evaluate the effectiveness of BHQ3 quenching of pyro photoactivity. As shown in Figure 2C, BHQ3 addition to PP_{MMP13} drastically decreased the fluorescence emission from the resulting $PP_{MMP13}B$ beacon when compared to the unquenched BHQ3-free PP_{MMP13} control. Fluorescence quenching efficiency of $PP_{MMP13}B$ relative to PP_{MMP13} was calculated to be $88.9 \pm 0.1\%$ ($n = 3$). Singlet oxygen generation was also successfully quenched through BHQ3 conjugation to PP_{MMP13} as evidenced through in solution SOSG assays

conducted across increasing light doses. As shown in Figure 2D, the SOSG-only control displayed a negligible increase in SOSG fluorescence background over the range of light doses tested. For unquenched PP_{MMP13}, a robust increase in SOSG fluorescence was observed with an increasing light dose, demonstrating light-dose enhanced $^1O_2$ generation. In contrast, a minimal increase in SOSG fluorescence was observed for $PP_{MMP13}B$ over increasing light doses. As such, $^1O_2$ generation was astoundingly silenced in $PP_{MMP13}B$ versus the unquenched PP_{MMP13} across all light doses. For example, at the highest light dose tested ($25\,J{\cdot}cm^{-2}$), PP_{MMP13} displayed a 24-fold increase in SOSG fluorescence compared to the light-free control, while the intact $PP_{MMP13}B$ only demonstrated a 2-fold increase, indicating a 12-fold silencing of photoreactivity in $PP_{MMP13}B$. To investigate the susceptibility of the beacon to photobleaching, pyro fluorescence signal of PP_{MMP13}, intact $PP_{MMP13}B$ and nonspecifically cleaved $PP_{MMP13}B$ (by Proteinase K) was

measured following light treatment (Figure 2E). No significant decrease in pyro fluorescence signal was observed across samples or light doses, indicating that PP_{MMP13}, $PP_{MMP13}B$, and its fragments are photostable, and photobleaching was not a factor in the observed quenching of $PP_{MMP13}B$ photoreactivity. Taken together, BHQ3 conjugation effectively quenched both pyro fluorescence and $^1O_2$ generation in the $PP_{MMP13}B$ beacon.

3.3. MMP-13-Triggered Activation of $PP_{MMP13}B$

Having confirmed that $PP_{MMP13}B$ in its intact state was fluorescently and photoreactively quenched, we next determined its ability to be activated by its target protease, MMP-13, in solution. $PP_{MMP13}B$ was incubated with MMP-13 at a 1:40 protease:beacon molar ratio at 37 °C (Figure 3A). Aliquots were removed from this incubated reaction mixture and measured on a spectrofluorometer over the course of 24 h, while uPLC-MS was used to validate beacon cleavage and identify cleavage products. We found that MMP-13 cleaved $PP_{MMP13}B$ into two fragments (Figure 3A,B): a pyro-GPLG fragment (4.36 min uPLC retention time) and a FRVGK-BHQ3 fragment (2.61 min uPLC retention time). These were identified based on the absorbance spectra and ESI mass spectra of each uPLC peak. The fragment associated with the 4.36 min retention time was identified as pyro-containing on account of its characteristic UV−vis spectrum (Figure 3Bii), while its associated peptide fragment was identified via ESI-MS (Figure 3Biii; m/z calcd for $C_{48}H_{58}N_8O_7$ $[M]^+$ 858.44, found m/z 859.4 $[M + H]^+$). The fragment associated with the 2.61 min peak was identified based on its characteristic BHQ3 absorbance spectrum (Figure 3Biv) and concordant ESI-MS (Figure 3Bv; m/z calcd for $C_{61}H_{81}N_{16}O_6^+$ $[M]^+$ 1133.65, found m/z 567.3 $[M + 2H]^{2+}$). This MMP-13-mediated $PP_{MMP13}B$ cleavage successfully restored pyro fluorescence. Kinetic characterization of the cleavage reaction over 2 h revealed that while $PP_{MMP13}B$ alone showed no change in fluorescence signal over the course of incubation, a linear increase in fluorescence signal was observed in the presence of MMP-13 (Figure S3). Fluorescence characterization of aliquots over the course of 24 h revealed that MMP-13 addition to $PP_{MMP13}B$ yielded strong pyro fluorescence spectra (Figure 3C). Integration and normalization of the associated fluorescence intensities yielded a logarithmic profile characteristic of enzyme progress curves (Figure 3D). After 24 h, a 13-fold increase in fluorescence signal was observed compared to the fully intact $PP_{MMP13}B$ at 0 h. About half of this fluorescence activation (7-fold increase) was reached in the first 3 h of $PP_{MMP13}B$ incubation with MMP-13. This $PP_{MMP13}B$ activation by MMP-13 was stronger and faster than what has been observed in literature for a commercial MMP fluorescent beacon.[27] These data together indicated that $PP_{MMP13}B$ was successfully and robustly cleaved by MMP-13, liberating pyro from BHQ3 and restoring pyro fluorescence signal. In doing so, these data validated the premise of designing and using $PP_{MMP13}B$ as a readout of pathological OA protease activity.

3.4. Cleavage Specificity of $PP_{MMP13}B$ toward Various MMPs

One of the postulated advancements in our beacon design was to generate an OA pathogenesis-activated beacon with higher selectivity to MMP-13 over other proteases. We thus characterized the specificity of $PP_{MMP13}B$ activation by various MMPs (MMP-1, -2, -3, -7, -8, -9, -10, -11, -12, and -13) and ADAMTSs (ADAMTS-4 and -5), a second class of proteases implicated in OA pathogenesis.[19] $PP_{MMP13}B$ was incubated alone or in combination with individual proteases. Each reaction was allowed to ensue for 24 h at 37 °C, at which point

fluorescence spectroscopy and uPLC-MS were conducted on reaction mixtures. Figure S4 displays the integrated fluorescence intensity of the protease and $PP_{MMP13}B$ reaction mixtures normalized to integrated intensities associated with $PP_{MMP13}B$ incubation alone. Compared to Proteinase K, which causes nonspecific but complete $PP_{MMP13}B$ cleavage (100% activation), MMP-13 and MMP-10 caused approximately 85% beacon activation. All other proteases demonstrated significantly lower protease activation compared to MMP-13 (one-way ANOVA, Tukey's test for multiple comparisons $p < 0.0001$, $n = 4$), though significant and appreciable (60%) activation of $PP_{MMP13}B$ was also caused by MMP-3 ($p < 0.0001$ versus $PP_{MMP13}B$ alone). The uPLC-MS profiles of the $PP_{MMP13}B$/protease reaction products (Figure S5) verified these observed trends in cleavage specificity. The uPLC traces of the MMP-13 and MMP-10 reactions demonstrated near complete eradication of the peak associated with intact $PP_{MMP13}B$ (retention time of 3.97 min), and the presence of strong peaks at retention times of 2.61 and 4.36 min, which were previously found, as shown in Figure 3, to be associated with FRVGK-BHQ3 and pyro-GLPLG fragments generated from peptide cleavage between the Gly and Phe residues. The MMP-3/beacon reaction also generated peaks associated with FRVGK-BHQ3 and pyro-GLPLG, but thes were similar in height to $PP_{MMP13}B$. Small amounts of cleavage fragments associated with MMP-9 and MMP-12 reactions were also observed by uPLC, but the corresponding beacon fluorescent activations were only 35 and 20%, respectively. These results suggest that $PP_{MMP13}B$ underwent site-specific cleavage that yielded beacon fluorescence activation with greatest specificity to MMP-13 and MMP-10 and to a lesser but still considerable extent to MMP-3.

Given the similarities in structure across MMPs, some $PP_{MMP13}B$ cleavage crosstalk between MMP-13, MMP-3, and MMP-10 is not altogether unexpected.[47] Nevertheless, consideration of off-target beacon activation is critical, especially for MMP-10 given its comparable cleavage of $PP_{MMP13}B$ to MMP-13. MMP-10 is typically not expressed in normal tissue aside from during skeletal development.[48] Instead, its expression is observed in response to injury (for example skin wound healing and bone fracture)[49,50] and systemic pathologies (most notably in atherosclerosis,[51] cancer invasion[52] and angiogenesis[53]). However, its gene expression in OA synovium and cartilage is 3−4 orders of magnitude lower than that of MMP-13.[50] Thus, off-target $PP_{MMP13}B$ activation by MMP-10 is of less concern at the joint site in the context of OA, and more relevant systemically. This concern can be mitigated through local administration of $PP_{MMP13}B$ via intraarticular injection. Unlike MMP-10, MMP-3 is expressed in osteoarthritic tissue. MMP-3 is responsible for the activation of other MMPs,[54] is upregulated in OA, is a driver of OA cartilage damage, and has a more differential expression between normal and early stage OA than MMP-13.[26,55,56] MMP-9, for which minor beacon activation was observed, is also upregulated in later stages of OA.[55] Thus, MMP-3's ability to cleave $PP_{MMP13}B$, and to a lesser extent MMP-9's cleavage abilities, is likely beneficial as an additional source of pathogenesis-activated imaging in an OA joint. Altogether, the activation profile of $PP_{MMP13}B$ was thus suitable for its continued exploration for OA applications.

3.5. Quantifying Cellular Uptake and Cytotoxicity of $PP_{MMP13}B$ in Patient-Derived Cells

One of the key parameters that could allow for more effective and versatile application of $PP_{MMP13}B$ in OA management is
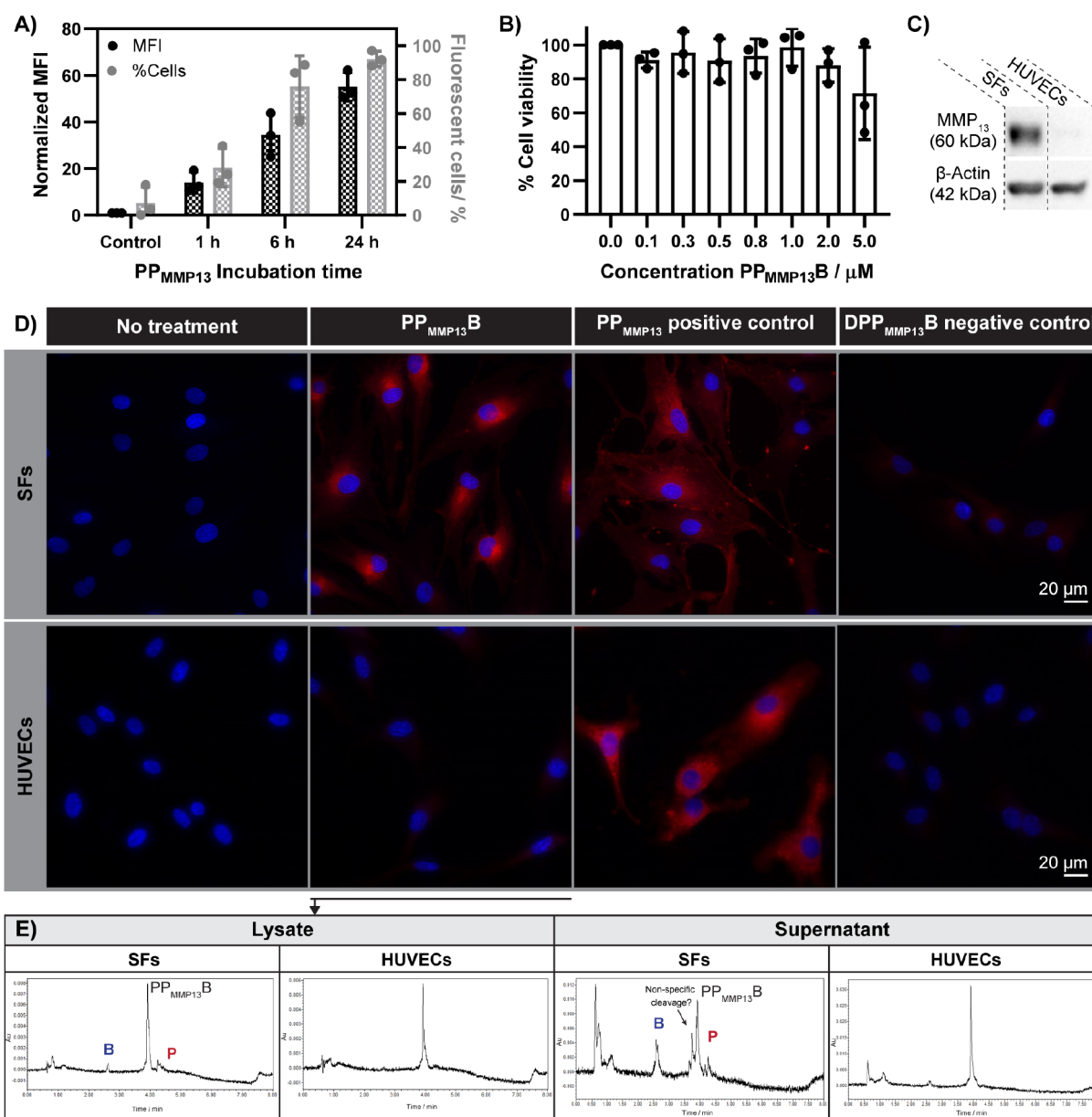
Figure 4. Efficient intracellular uptake of beacon in primary fibroblast-like synoviocytes (SFs) was demonstrated by administrating fluorescence positive control PP$_{MMP13}$ and quantifying pyro uptake with flow cytometry (A). This uptake did not yield any significant toxicity to SFs at varying porphyrin doses (B). Western blots of patient-derived SFs demonstrated high MMP-13 expression when compared to HUVECs (C). Fluorescence microscopy (red: Cy5 620/60 ex, 665 long-pass em, 200 ms exposure SFs, 1500 ms exposure HUVECs; blue: DAPI 375/28 ex, 460/50 em) was conducted to characterize beacon uptake and activation following 24 h incubation (2.5 μM PP$_{MMP13}$B, PP$_{MMP13}$, or DPP$_{MMP13}$B) with SFs or HUVECs (D). PP$_{MMP13}$ (no quencher) was used as a positive control, and DPP$_{MMP13}$B (synthesized with a D-amino acid sequence) was used as an uncleavable negative control. PP$_{MMP13}$B activation was observed in SFs but not in HUVECs. This corresponded to more obvious observation of cleaved PP$_{MMP13}$B (P = porphyrin fragment, B = BHQ3 fragment) within supernatants and lysates of PP$_{MMP13}$B-treated SFs than PP$_{MMP13}$B-treated HUVECs (E).

effective cellular uptake within cartilage and synovium. Thus, we next explored this feasibility in vitro by characterizing the cellular uptake profile of PP$_{MMP13}$ in OA patient-derived fibroblast-like synoviocytes (SFs; Figure 4A and Figure S6) and chondrocytes (Figures S6 and S7A). The "always on" fluorescence of PP$_{MMP13}$ allowed it to serve as a better substrate to quantify cellular delivery via flow cytometry as it removed the confounding matter of beacon quenching skewing such quantification. Cells were treated with 1 μM of PP$_{MMP13}$ for varying amounts of time, and the percentage of cells stained with pyro and overall mean fluorescence intensity (MFI) were determined. Both human OA joint tissue cell types demonstrated similar PP$_{MMP13}$ uptake

profiles. After 1 h of incubation, $30 \pm 10\%$ of SFs and $38 \pm 2\%$ of chondrocytes exhibited PP$_{MMP13}$ uptake, yielding a 14 ± 5- and 12 ± 2-fold increase in MFI over controls, respectively. After 6 h of incubation, the majority of cells exhibited PP$_{MMP13}$ uptake, with 80% of SFs and chondrocytes demonstrating pyro fluorescence. By 24 h, $92 \pm 5\%$ of SFs and $92 \pm 3\%$ of chondrocytes exhibited PP$_{MMP13}$ fluorescence signal, yielding a 55 ± 6 and 38 ± 11 times higher MFI over controls, respectively. This high cellular uptake coincided with insignificant PP$_{MMP13}$B cell toxicity at doses under 2 μM in both SFs (Figure 4B) and chondrocytes (Figure S7B). Additionally, PP$_{MMP13}$B did not impair SF or chondrocyte cellular responses to stimulation
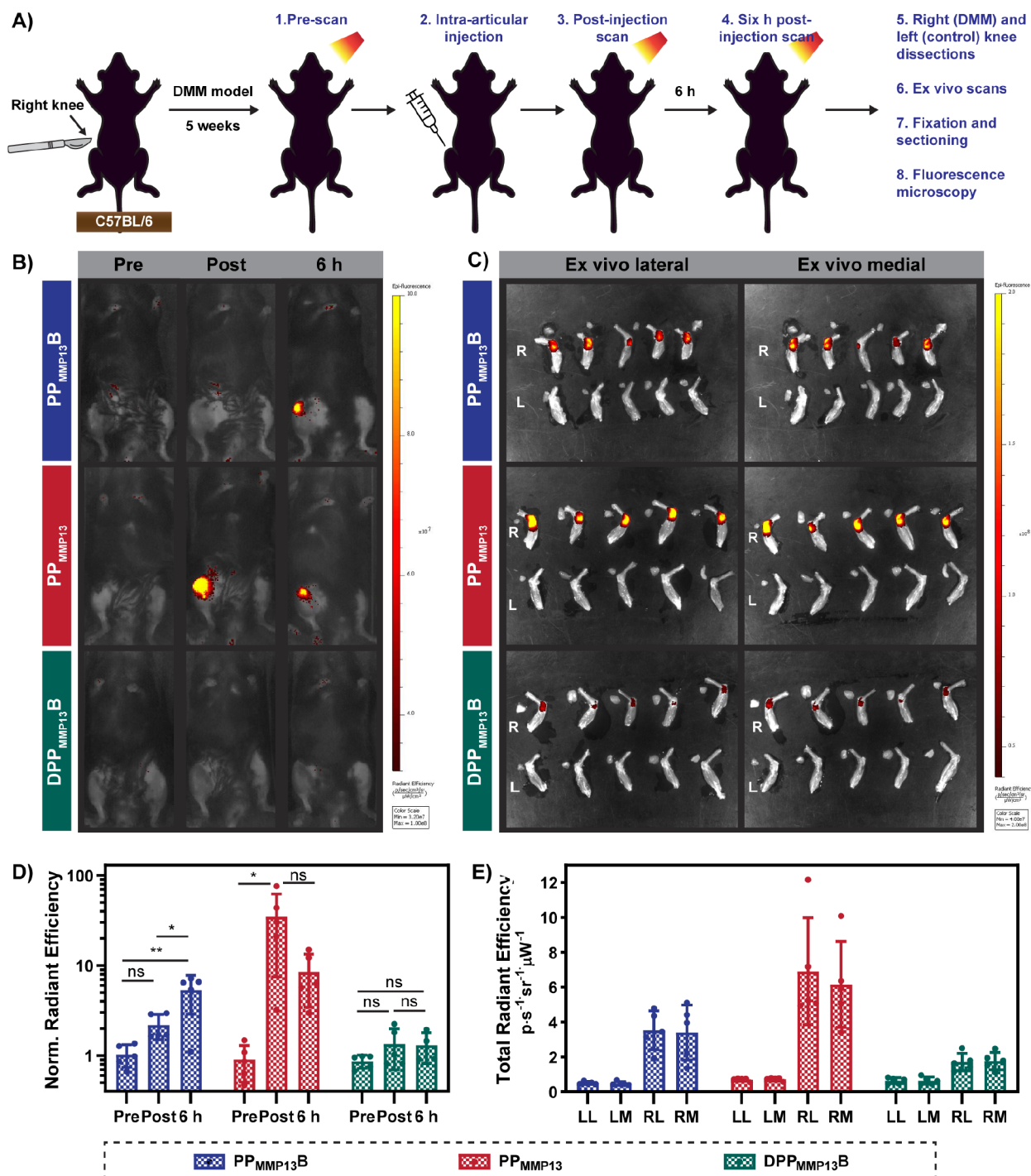
Figure 5. In vivo assessment of PP$_{MMP13}$B fluorescence activation was conducted in a DMM model of OA (A). The right knees of mice were surgically destabilized. After 5 weeks, the right knees received intra-articular injections of 1 nmol of PP$_{MMP13}$, PP$_{MMP13}$B, or DPP$_{MMP13}$B (n = 5 each), while the left knees served as no treatment PBS controls. In vivo fluorescence imaging (B) was conducted (IVIS Spectrum, 675 nm ex, 720 nm em, 6 s exposure) prior to injection, directly after injection and 6 h postinjection. Mice were then euthanized and dissected to harvest right (R) and left (L) knee joints as well as surrounding muscle. Ex vivo fluorescence imaging (C) was conducted on the lateral and medial aspects of the joints (IVIS Spectrum, 675 nm ex, 720 nm em, 4 s exposure). ROI analysis of fluorescence images was conducted over the knee joint for in vivo images acquired prior to injection, directly after injection and 6 h postinjection (D). One-way ANOVA was conducted among each treatment group with corrected significance denoted as *p < 0.0332, **p < 0.0021 or ns for no significant difference. ROI analysis was also conducted over the dissected bone/joint (muscle excluded) for ex vivo images (E) acquired viewing the lateral (LL = left knee lateral, RL = right knee lateral) or medial (LM = left knee medial, RM = right knee medial) aspects of the knee. All ex vivo right knee fluorescence intensities were significantly higher than their associated left knees in each treatment group (p = 0.007 to 0.0024).

(Figure S7C and Figure S8). Such effective cellular delivery paired with low cytotoxicity is reassuring for the intra-articular delivery of PP$_{MMP13}$B.

3.6. PP$_{MMP13}$B Activation by MMP-13 Expressing SFs In Vitro

To test the potential of PP$_{MMP13}$B for MMP-13 enabled imaging, we compared PP$_{MMP13}$B activation in MMP-13 expressing SFs to

negligibly expressing HUVECs. For this in vitro study, we focused primarily on activation within SFs since MMP-13 upregulation in OA, and across OA stages is particularly strongly observed in the synovium.[25] The MMP-13 relative expression profiles of SFs and HUVECs were confirmed via Western blotting (Figure 4C). SFs and HUVECs were treated with either $PP_{MMP13}B$, PP_{MMP13} (as a positive control) or $DPP_{MMP13}B$ (a negative control to rule out nonspecific cleavage). Cells were imaged by fluorescence microscopy to visualize intracellular activation. As shown in Figure 4D, after 24 h of incubation with the unquenched PP_{MMP13}, both HUVECs and MMP-13 + SFs exhibited bright intracellular pyro fluorescence, confirming strong cellular uptake. On the other hand, treatment with $DPP_{MMP13}B$ yielded negligible fluorescence in both cell lines, demonstrating minimal background beacon cleavage and activation. $PP_{MMP13}B$ in contrast to both positive and negative controls demonstrated successful fluorescent activation in MMP-13 + SFs but not in HUVECs, thus showing MMP-13 cell expression-dependent intracellular fluorescence activation. Collectively, these results demonstrated $PP_{MMP13}B$ underwent effective MMP-13-enabled, specific fluorescent activation.

To verify that this cell-specific activation was from differential beacon cleavage between the cell types, supernatants and lysates of SFs and HUVECs treated with $PP_{MMP13}B$ for 24 h were collected and characterized by uPLC (Figure 4E). While the cell lysate of HUVECs was associated with a large single uPLC peak corresponding to intact $PP_{MMP13}B$ and no other concretely discernible peaks, the cell lysate from SFs displayed 3 clear uPLC peaks. These corresponded to the MMP13-cleaved BHQ3 fragment (2.6 min), intact $PP_{MMP13}B$ (4 min), and MMP13-cleaved pyro fragment (4.3 min) uPLC profiles observed from in solution MMP-13 cleavage studies. This demonstrated successful intracellular cleavage of $PP_{MMP13}B$ in SFs but not in HUVECs, in line with fluorescence microscopy results. As MMP-13 is secreted into synovial fluid in OA, we also characterized $PP_{MMP13}B$ cleavage in the cell media supernatants where extracellular MMP-13 would be excreted in an in vitro setting. Little $PP_{MMP13}B$ cleavage was observed in the HUVEC supernatants while substantial cleavage was observed in the SF supernatants. These in vitro data together indicated that (1) $PP_{MMP13}B$ can enter human SFs and can subsequently be cleaved and activated into fluorescent fragments, (2) there was a possibility of slight cleavage of $PP_{MMP13}B$ in HUVECs from its negligible but not absent levels of MMP-13 expression or from off-target HUVEC MMPs,[49] and (3) in addition to facilitating MMP-13 expression-dependent intracellular $PP_{MMP13}B$ activation, SFs also excreted proteases that caused extracellular $PP_{MMP13}B$ cleavage, yielding fragments in line with those expected from MMP-13-enabled cleavage. Due to experimental limitations, quantification of extracellular MMP-13 was not performed in this study. Nevertheless, based on these data, extracellular MMP secretion will likely play a critical role in beacon activation in synovial fluid. This could enhance the fluorescence imaging capabilities of $PP_{MMP13}B$ and also create a pathway for future studies in which $PP_{MMP13}B$ could be applied ex vivo to human synovial fluid in varying disease stages. These conditions would not only provide a meaningful demonstration of selective $PP_{MMP13}B$ activation in diseased over healthy synovial fluid samples but also the results could subsequently be correlated to disease severity (i.e., early vs late stage OA). Furthermore, although we focused on MMP-13 expression in these in vitro studies, it is possible that other MMPs, particularly MMP-3 due to its established $PP_{MMP13}B$ cleavage efficacy and

OA tissue expression profile, played a role in $PP_{MMP13}B$ cleavage and activation. As discussed above this is likely beneficial in the context of $PP_{MMP13}B$ applications in OA.

3.7. $PP_{MMP13}B$ Localization and Activation in DMM-Induced OA Mice Knee Joints

To explore whether the in vitro cell uptake and activation profiles of $PP_{MMP13}B$ translated to an in vivo setting, we studied the beacon's intra-articular distribution and fluorescence imaging capabilities in a destabilization of the medial meniscus joint model of OA. Experiments were conducted 5 weeks after DMM surgeries took place on the right knees of C57BL/6 mice, a timeline consistent with mild to moderate OA. The experimental plan depicted in Figure 5A was followed for three groups of mice (n = 5 per group) receiving intra-articular injections of either (1) $PP_{MMP13}B$, (2) PP_{MMP13}, or (3) $DPP_{MMP13}B$ in their right knee, with the left knee serving as an internal control for background fluorescence. Whole body fluorescence images were taken prior to injection, directly after injection and 6 h postinjection, at which point mice were euthanized and knee joints were excised for ex vivo fluorescence imaging from both lateral and medial viewpoints. Joints were then fixed and cryosectioned for fluorescence microscopy.

As shown in Figure 5B,D, the positive fluorescent control, PP_{MMP13}, exhibited strong fluorescence (34 ± 20-fold increase compared to prescan baseline, p = 0.0149) at the DMM knee joint directly after injection. This fluorescent signal decreased 75 ± 6% in strength over the course of 6 h, likely due to synovial clearance of PP_{MMP13}. However, as the time constant (τ) for synovial clearance of similarly sized agents in mice is 2.85 h,[57] the persistence of strong fluorescence signal at the knee joint site at 6 h postinjection (9 ± 3-fold higher than prescan baseline) indicated some tissue retention of PP_{MMP13}. This was a positive finding given that tissue retention in OA knee joints is paramount for the successful biomedical application of our tailored molecular beacon whether for imaging, PDT, or drug delivery purposes. Unlike the "always on" PP_{MMP13} control, $PP_{MMP13}B$ did not exhibit visible fluorescent signal at the DMM knee joint directly after injection. ROI analysis demonstrated a 2.1 ± 0.3-fold increase in signal over the prescan, but this was found to be statistically insignificant (p = 0.3905) and only represented 6% of the fluorescence signal intensity observed for PP_{MMP13} directly postinjection. However, over the course of 6 h, strong fluorescent signal from $PP_{MMP13}B$ was generated at the injection site (6 ± 3-fold increase over baseline, p = 0.0016), with 63% fluorescence signal activated compared to PP_{MMP13} at the same time point. This demonstrated successful $PP_{MMP13}B$ activation in the DMM OA knee joint model. This activation was peptide sequence-specific as evident from a lack of specific fluorescent activation of $DPP_{MMP13}B$, whose in vivo fluorescence signal, unlike $PP_{MMP13}B$, did not significantly change directly postinjection to 6 h postinjection (p = 0.9923) or above baseline (p = 0.2945 post, p = 0.3883 6 h). Ex vivo imaging of $DPP_{MMP13}B$ did however demonstrate some unquenched background fluorescence (2.7 ± 0.5-fold increase over PBS control p = 0.0019 lateral aspect, 2.8 ± 0.5-fold increase over PBS control p = 0.0012 medial aspect). This $DPP_{MMP13}B$ background fluorescence could be from nonspecific beacon cleavage, but due to any lack of fluorescence intensity change between postinjection and 6 h imaging time points in vivo, a larger contributor was likely the presence of unquenched beacon (recall $PP_{MMP13}B$ exhibited high but incomplete fluorescence quenching efficiency of 90%). However, like in vivo fluorescence
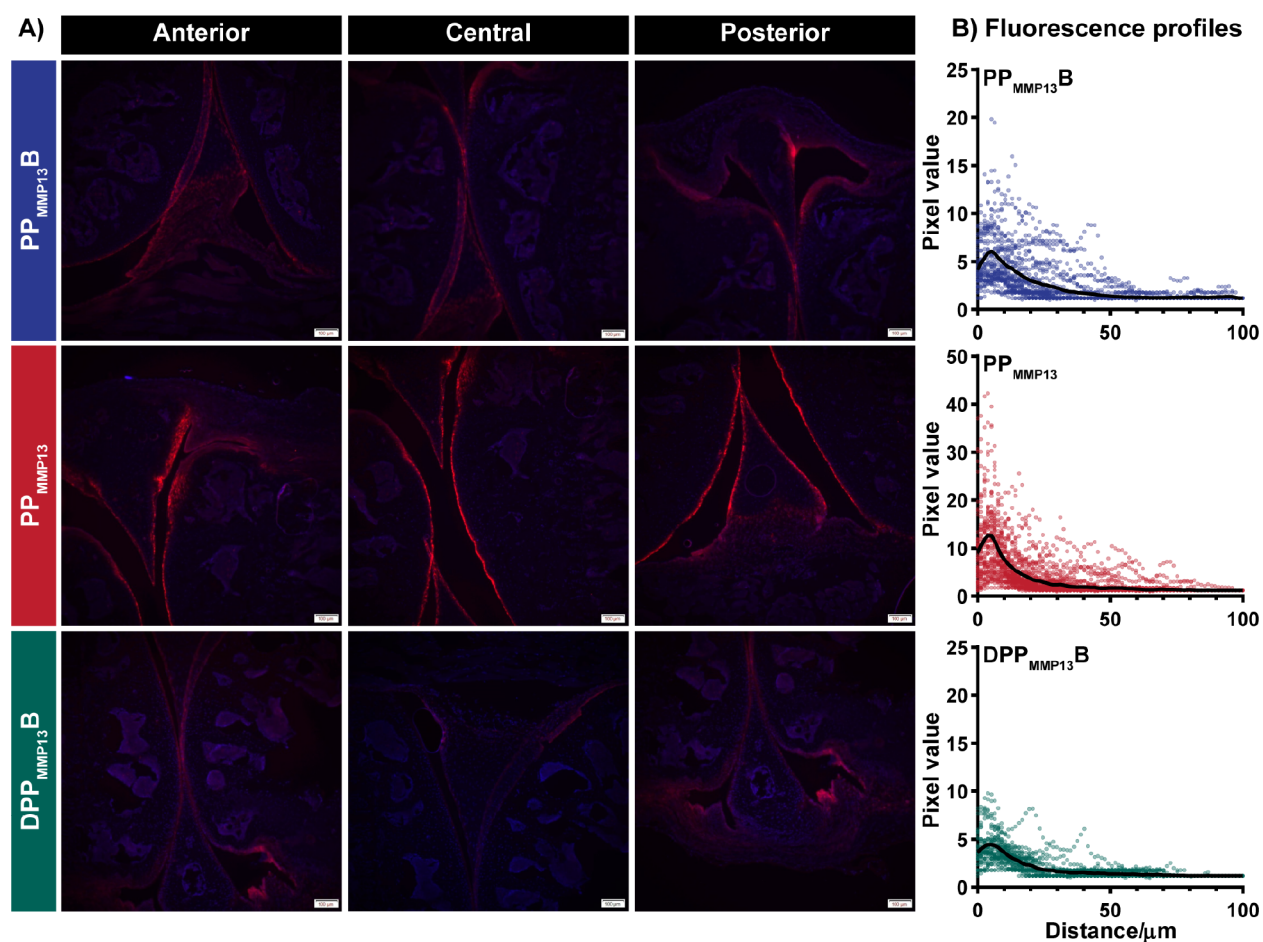
Figure 6. Dissected knee joints were subjected to fixation, cryosectioning and fluorescence microscopy to visualize $PP_{MMP13}B$ activation and porphyrin localization within the articular cartilage (A). Images were taken along the entire length of the joint, with posterior, central and anterior aspects of these lengths shown. ImageJ analysis of fluorescence profiles was conducted by drawing lines perpendicular to the articular cartilage along the entire cartilage depth at approximately $50-75$ μm intervals. Multiplot analysis was conducted and plots for each linear profile were combined (B). Individual pixel values (circular symbols) and the averaged mean pixel value per distance (black line) are shown. Scale bar = 100 μm. Microscopy acquisition parameters: pyro: Cy5 channel 620/60 nm excitation, 665 nm long-pass emission, 750 ms exposure; DAPI: 375/28 nm excitation, 460/50 nm emission, 500 ms exposure.

scans, $PP_{MMP13}B$ and PP_{MMP13} exhibited stronger visible fluorescence signal than $DPP_{MMP13}B$, signals that were, respectively, 7 ± 3 and 9 ± 3-fold higher than PBS controls imaged from the medial aspect. Together, these data demonstrated that $PP_{MMP13}B$ underwent sequence-specific fluorescence activation in a mouse model of OA, yielding strong in vivo and ex vivo fluorescence imaging contrast. In doing so, these in vivo data validated the potential of $PP_{MMP13}B$ as an activatable OA imaging probe.

Fluorescence microscopy of the knee joint sections was conducted to discern the microscopic locale of PP_{MMP13} tissue retention and $PP_{MMP13}B$ activation. As can be seen in Figure 6A, PP_{MMP13} delivery and $PP_{MMP13}B$ delivery/activation occurred along the entire surface of the articular cartilage, synovium, and menisci. This data demonstrated that joint-wide uptake and activation of $PP_{MMP13}B$ at a microscopic level could yield macroscopically robust fluorescence contrast in vivo at OA joint sites. As expected from in vivo and ex vivo fluorescence imaging studies, microscopic fluorescence intensities decreased in order from $PP_{MMP13} > PP_{MMP13}B > DPP_{MMP13}B$, where a signal observed in knee joints treated with $DPP_{MMP13}B$ was weak but still presented in the same pattern as PP_{MMP13} and $PP_{MMP13}B$. Fluorescence profile mapping demonstrated that $PP_{MMP13}B$ and

PP_{MMP13} impressively reached a depth of 50 μm within articular cartilage, which corresponded to approximately 50% of the entire length of the articular cartilage and within the chondrocyte-dense regions. This excellent intra-articular distribution renders these agents promising candidates to study in the future for drug delivery, and in the case of $PP_{MMP13}B$, joint-wide PDT.

Altogether, our in vivo data validated the activatable nature of $PP_{MMP13}B$ in OA-afflicted joint tissue as well as its robust delivery to articular cartilage and synovium. In doing so, this study sets the foundation for continued exploration and optimization of $PP_{MMP13}B$ for pathology-driven OA molecular imaging and treatment. In this proof-of-concept study, we demonstrated the feasibility of using $PP_{MMP13}B$ to image OA joint tissue. To better characterize whether $PP_{MMP13}B$ is selectively activated by diseased tissue, future application studies would benefit from comparison of $PP_{MMP13}B$ fluorescence activation in uninjured versus diseased OA joints, and over a greater number of postinjection time-points. This would confirm the platform's disease-specific imaging potential and allow definition of fluorescence and time thresholds for identifying diseased tissue specifically and sensitively. Should higher specificity be required, optimization of beacon design

could be achieved using strategies that increase beacon quenching efficiency and completely silence the intact beacon's photoactivity (such as the use of polycation–polyanion "zipper" structure designs[58]). Additionally, the $PP_{MMP13}B$ platform can easily be expanded to target other proteases implicated in OA. For example, ADAMTs form another important class of proteases implicated in OA pathogenesis[19] that could be used for beacon activation in future studies. These optimization strategies could address the background fluorescence we observed from the uncleavable D-peptide variant of $PP_{MMP13}B$, ensuring that fluorescence signal is better associated with joint pathology. A more selective $PP_{MMP13}B$ would also minimize off-target photoreactivity in the context of OA PDT applications. The intra-articular distribution of $PP_{MMP13}B$ warrants such future therapeutic application. The robust uptake and retention of $PP_{MMP13}B$ and unquenched PP_{MMP13} within articular cartilage could be leveraged to overcome the existing challenges of delivering disease-modifying drugs to chondrocytes. Specifically, the $PP_{MMP13}B$ synthesis protocol could be modified to conjugate such drugs to the C-terminal of PP_{MMP13} to form a pro-drug with potentially higher delivery efficacy than free drug. The ubiquitous intra-articular delivery of $PP_{MMP13}B$ also strengthens its promise as an activatable PDT agent for whole-joint OA therapy. With the setting of the foundation of $PP_{MMP13}B$ in this study, these multitude of future application explorations are now viable.

4. CONCLUSIONS

This study set out to design, synthesize and evaluate a new MMP-susceptible molecular beacon with targeted OA imaging, drug delivery and therapeutic potential. The innovation in this molecular beacon design lay in the use of a peptide substrate with increased specificity to OA-relevant metalloproteases compared to commercial beacons, and the inclusion of porphyrin as the beacon fluorophore, which uniquely renders the beacon inherently multimodal and theranostic. We synthesized and investigated the activatable nature of this prototype beacon, $PP_{MMP13}B$. Upon MMP-13 exposure, $PP_{MMP13}B$ demonstrated a near 13-fold increase in porphyrin fluorescence. The beacon was found to be nontoxic in vitro at doses up to 2 μM against OA patient-derived chondrocytes and fibroblast-like synoviocytes (SFs). $PP_{MMP13}B$ underwent MMP-13 expression-dependent fluorescence activation in vitro in human SFs, which translated to successful activation (63%) 6 h postinjection in OA-inflicted mouse knee joints in vivo, yielding strong activatable fluorescence contrast at the diseased knee joint. The beacon was additionally found to facilitate intra-articular accumulation of porphyrin within deep articular cartilage, synovium and menisci. Altogether, this study validated $PP_{MMP13}B$ as an activatable probe with OA molecular imaging capabilities. Its activatable nature and tissue-penetrating abilities also opens avenues that explore $PP_{MMP13}B$ for targeted OA PDT and delivery of otherwise impermeable disease-modifying drugs to articular cartilage. This study thus builds a foundation for the introduction of new biomolecular, pathogenesis-driven OA management strategies with potential to overcome current limitations in structural imaging and symptomatic OA therapies.

■ ASSOCIATED CONTENT

ⓈⒾ Supporting Information

The Supporting Information is available free of charge at https://pubs.acs.org/doi/10.1021/cbmi.3c00005.

Schematic of $PP_{MMP13}B$ synthesis (Figure S1); characterization of D-$PP_{MMP13}B$ (Figure S2); real-time monitoring of $PP_{MMP13}B$ cleavage by MMP13 (Figure S3); enzyme specific cleavage of $PP_{MMP13}B$ (Figure S4); uPLC profiles of $PP_{MMP13}B$ cleavage solutions (Figure S5); PP_{MMP13} uptake flow cytometry fluorescence histograms (Figure S6); characterization of primary patient-derived chondrocytes treated with PP_{MMP13} or $PP_{MMP13}B$ (Figure S7); PP_{MMP13} effect on SF stimulation (Figure S8) (PDF)

■ AUTHOR INFORMATION

Corresponding Authors

Juan Chen — *Princess Margaret Cancer Centre, University Health Network, Toronto, ON M5G 1L7, Canada;* Email: juan.chen@uhnresearch.ca

Mohit Kapoor — *Schroeder Arthritis Institute, University Health Network, Toronto, ON M5T 0S8, Canada; Krembil Research Institute, University Health Network, Toronto, ON M5T 0S8, Canada;* Email: mohit.kapoor@uhnresearch.ca

Gang Zheng — *Princess Margaret Cancer Centre, University Health Network, Toronto, ON M5G 1L7, Canada; Institute of Biomedical Engineering, University of Toronto, Toronto, ON M5S 3G9, Canada; Department of Medical Biophysics, University of Toronto, Toronto, ON M5G 1L7, Canada;* ⓘ orcid.org/0000-0002-0705-7398; Email: gang.zheng@uhnresearch.ca

Authors

Connor Walsh — *Princess Margaret Cancer Centre, University Health Network, Toronto, ON M5G 1L7, Canada; Institute of Biomedical Engineering, University of Toronto, Toronto, ON M5S 3G9, Canada*

Maneesha A. Rajora — *Princess Margaret Cancer Centre, University Health Network, Toronto, ON M5G 1L7, Canada; Institute of Biomedical Engineering, University of Toronto, Toronto, ON M5S 3G9, Canada*

Lili Ding — *Princess Margaret Cancer Centre, University Health Network, Toronto, ON M5G 1L7, Canada*

Sayaka Nakamura — *Schroeder Arthritis Institute, University Health Network, Toronto, ON M5T 0S8, Canada; Krembil Research Institute, University Health Network, Toronto, ON M5T 0S8, Canada*

Helal Endisha — *Schroeder Arthritis Institute, University Health Network, Toronto, ON M5T 0S8, Canada; Krembil Research Institute, University Health Network, Toronto, ON M5T 0S8, Canada*

Jason Rockel — *Schroeder Arthritis Institute, University Health Network, Toronto, ON M5T 0S8, Canada; Krembil Research Institute, University Health Network, Toronto, ON M5T 0S8, Canada*

Complete contact information is available at:
https://pubs.acs.org/10.1021/cbmi.3c00005

Author Contributions

[#]C.W. and M.A.R. are co-first authors.

Notes

The authors declare no competing financial interest.

■ ACKNOWLEDGMENTS

■ REFERENCES

(1) Long, H.; Liu, Q.; Yin, H.; Wang, K.; Diao, N.; Zhang, Y.; Lin, J.; Guo, A. Prevalence Trends of Site-Specific Osteoarthritis from 1990 to 2019: Findings from the Global Burden of Disease Study 2019. *Arthritis Rheumatol* **2022**, *74*, 1172−1183.

(2) Bitton, R. The Economic Burden of Osteoarthritis. *Am. J. Manag. Care* **2009**, *15*, S230−S235.

(3) Turkiewicz, A.; Petersson, I. F.; Bjork, J.; Hawker, G.; Dahlberg, L. E.; Lohmander, L. S.; Englund, M. Current and Future Impact of Osteoarthritis on Health Care: A Population-Based Study with Projections to Year 2032. *Osteoarthr Cartil* **2014**, *22*, 1826−1832.

(4) Katz, J. N.; Arant, K. R.; Loeser, R. F. Diagnosis and Treatment of Hip and Knee Osteoarthritis: A Review. *JAMA* **2021**, *325*, 568−578.

(5) Chalian, M.; Roemer, F. W.; Guermazi, A. Advances in Osteoarthritis Imaging. *Curr. Opin Rheumatol* **2023**, *35*, 44−54.

(6) Guermazi, A.; Roemer, F. W.; Haugen, I. K.; Crema, M. D.; Hayashi, D. Mri-Based Semiquantitative Scoring of Joint Pathology in Osteoarthritis. *Nat. Rev. Rheumatol* **2013**, *9*, 236−251.

(7) Mahmoudian, A.; Lohmander, L. S.; Mobasheri, A.; Englund, M.; Luyten, F. P. Early-Stage Symptomatic Osteoarthritis of the Knee - Time for Action. *Nat. Rev. Rheumatol* **2021**, *17*, 621−632.

(8) Loeser, R. F.; Goldring, S. R.; Scanzello, C. R.; Goldring, M. B. Osteoarthritis: A Disease of the Joint as an Organ. *Arthritis Rheum* **2012**, *64*, 1697−1707.

(9) Heinegård, D.; Saxne, T. The Role of the Cartilage Matrix in Osteoarthritis. *Nat. Rev. Rheumatol* **2011**, *7*, 50−56.

(10) Goldring, M. B.; Marcu, K. B. Cartilage Homeostasis in Health and Rheumatic Diseases. *Arthritis Res. Ther* **2009**, *11*, 224.

(11) Andriacchi, T. P.; Mündermann, A. The Role of Ambulatory Mechanics in the Initiation and Progression of Knee Osteoarthritis. *Curr. Opin Rheumatol* **2006**, *18*, 514−518.

(12) Kapoor, M.; Martel-Pelletier, J.; Lajeunesse, D.; Pelletier, J. P.; Fahmi, H. Role of Proinflammatory Cytokines in the Pathophysiology of Osteoarthritis. *Nat. Rev. Rheumatol* **2011**, *7*, 33−42.

(13) Mengshol, J. A.; Vincenti, M. P.; Coon, C. I.; Barchowsky, A.; Brinckerhoff, C. E. Interleukin-1 Induction of Collagenase 3 (Matrix Metalloproteinase 13) Gene Expression in Chondrocytes Requires P38, C-Jun N-Terminal Kinase, and Nuclear Factor Kb: Differential Regulation of Collagenase 1 and Collagenase 3. *Arthritis Rheum* **2000**, *43*, 801−811.

(14) Felson, D. T.; Lawrence, R. C.; Dieppe, P. A.; Hirsch, R.; Helmick, C. G.; Jordan, J. M.; Kington, R. S.; Lane, N. E.; Nevitt, M. C.; Zhang, Y.; et al. Osteoarthritis: New Insights. Part 1: The Disease and Its Risk Factors. *Ann. Int. Med.* **2000**, *133*, 635−646.

(15) Lohmander, L. S.; Saxne, T.; Heinegård, D. K. Release of Cartilage Oligomeric Matrix Protein (Comp) into Joint Fluid after Knee Injury and in Osteoarthritis. *Ann. Rheum Dis* **1994**, *53*, 8−13.

(16) Scanzello, C. R.; Goldring, S. R. The Role of Synovitis in Osteoarthritis Pathogenesis. *Bone* **2012**, *51*, 249−257.

(17) Frost, H. Perspective: Genetic and Hormonal Roles in Bone Disorders: Insights of an Updated Bone Physiology. *J. Musculoskelet. Neuronal Interact.* **2003**, *3*, 118−135.

(18) van der Kraan, P. M.; van den Berg, W. B. Osteophytes: Relevance and Biology. *Osteoarthr Cartil* **2007**, *15*, 237−244.

(19) Troeberg, L.; Nagase, H. Proteases Involved in Cartilage Matrix Degradation in Osteoarthritis. *Biochimica et Biophysica Acta - Proteins and Proteomics* **2012**, *1824*, 133−145.

(20) Nagase, H.; Visse, R.; Murphy, G. Structure and Function of Matrix Metalloproteinases and Timps. *Cardiovasc. Res.* **2006**, *69*, 562−573.

(21) Mitchell, P. G.; Magna, H. A.; Reeves, L. M.; Lopresti-Morrow, L. L.; Yocum, S. A.; Rosner, P. J.; Geoghegan, K. F.; Hambor, J. E. Cloning, Expression, and Type Ii Collagenolytic Activity of Matrix Metalloproteinase-13 from Human Osteoarthritic Cartilage. *J. Clin Invest* **1996**, *97*, 761−768.

(22) Billinghurst, R. C.; Dahlberg, L.; Ionescu, M.; Reiner, A.; Bourne, R.; Rorabeck, C.; Mitchell, P.; Hambor, J.; Diekmann, O.; Tschesche, H.; et al. Enhanced Cleavage of Type Ii Collagen by Collagenases in Osteoarthritic Articular Cartilage. *J. Clin Invest* **1997**, *99*, 1534−1545.

(23) Little, C. B.; Barai, A.; Burkhardt, D.; Smith, S. M.; Fosang, A. J.; Werb, Z.; Shah, M.; Thompson, E. W. Matrix Metalloproteinase 13-Deficient Mice Are Resistant to Osteoarthritic Cartilage Erosion but Not Chondrocyte Hypertrophy or Osteophyte Development. *Arthritis Rheum* **2009**, *60*, 3723−3733.

(24) Bau, B.; Gebhard, P. M.; Haag, J.; Knorr, T.; Bartnik, E.; Aigner, T. Relative Messenger Rna Expression Profiling of Collagenases and Aggrecanases in Human Articular Chondrocytes in Vivo and in Vitro. *Arthritis Rheum* **2002**, *46*, 2648−2657.

(25) Zhao, Q.-H.; Lin, L.-P.; Guo, Y.-X.; Zou, R.; Wang, Z.; Shi, Z.-P.; Lin, F.-Q. Matrix Metalloproteinase-13, Nf-Kappab P65 and Interleukin-1beta Are Associated with the Severity of Knee Osteoarthritis. *Exp Ther Med.* **2020**, *19*, 3620−3626.

(26) Jarecki, J.; Malecka-Masalska, T.; Kosior-Jarecka, E.; Widuchowski, W.; Krasowski, P.; Gutbier, M.; Dobrzynski, M.; Blicharski, T. Concentration of Selected Metalloproteinases and Osteocalcin in the Serum and Synovial Fluid of Obese Women with Advanced Knee Osteoarthritis. *Int. J. Environ. Res. Public Health* **2022**, *19*, 3530.

(27) Leahy, A. A.; Esfahani, S. A.; Foote, A. T.; Hui, C. K.; Rainbow, R. S.; Nakamura, D. S.; Tracey, B. H.; Mahmood, U.; Zeng, L. Analysis of the Trajectory of Osteoarthritis Development in a Mouse Model by Serial near-Infrared Fluorescence Imaging of Matrix Metalloproteinase Activities. *Arthritis Rheumatol* **2015**, *67*, 442−453.

(28) Rasmussen, F. H.; Yeung, N.; Kiefer, L.; Murphy, G.; Lopez-Otin, C.; Vitek, M. P.; Moss, M. L. Use of a Multiple-Enzyme/Multiple-Reagent Assay System to Quantify Activity Levels in Samples Containing Mixtures of Matrix Metalloproteinases. *Biochemistry* **2004**, *43*, 2987−2995.

(29) Fields, G. B. Using Fluorogenic Peptide Substrates to Assay Matrix Metalloproteinases. *Methods in Molecular Biology*; Springer: Clifton, NJ 2010; Vol. 622, pp 393−433.

(30) Rosenfeld, A.; Morgan, J.; Goswami, L. N.; Ohulchanskyy, T.; Zheng, X.; Prasad, P. N.; Oseroff, A.; Pandey, R. K. Photosensitizers Derived from 132-Oxo-Methyl Pyropheophorbide-A: Enhanced Effect of Indium(Iii) as a Central Metal in in Vitro and in Vivo Photosensitizing Efficacy. *Photochem. Photobiol.* **2006**, *82*, 626−634.

(31) Liu, T. W.; MacDonald, T. D.; Shi, J.; Wilson, B. C.; Zheng, G. Intrinsically Copper-64-Labeled Organic Nanoparticles as Radiotracers. *Angew. Chem., Int. Ed. Engl.* **2012**, *51*, 13128−13131.

(32) MacDonald, T. D.; Liu, T. W.; Zheng, G. An Mri-Sensitive, Non-Photobleachable Porphysome Photothermal Agent. *Angew. Chem., Int. Ed. Engl.* **2014**, *53*, 6956−6959.

(33) Chen, J.; Stefflova, K.; Niedre, M. J.; Wilson, B. C.; Chance, B.; Glickson, J. D.; Zheng, G. Protease-Triggered Photosensitizing Beacon Based on Singlet Oxygen Quenching and Activation. *J. Am. Chem. Soc.* **2004**, *126*, 11450−11451.

(34) Kirdaite, G.; Lange, N.; Busso, N.; Van Den Bergh, H.; Kucera, P.; So, A. Protoporphyrin Ix Photodynamic Therapy for Synovitis. *Arthritis Rheum* **2002**, *46*, 1371−1378.

(35) Zhao, C.; Ur Rehman, F.; Yang, Y.; Li, X.; Zhang, D.; Jiang, H.; Selke, M.; Wang, X.; Liu, C. Bio-Imaging and Photodynamic Therapy with Tetra Sulphonatophenyl Porphyrin (Tspp)-Tio2 Nanowhiskers: New Approaches in Rheumatoid Arthritis Theranostics. *Sci. Rep* **2015**, *5*, 11518.

(36) Won, E.; Akens, M. K.; Hardisty, M. R.; Burch, S.; Bisland, S. K.; Yee, A. J. M.; Wilson, B. C.; Whyne, C. M. Effects of Photodynamic Therapy on the Structural Integrity of Vertebral Bone. *Spine (Phila Pa 1976)* **2010**, *35*, 272−277.

(37) Lo, V. C. K.; Akens, M. K.; Wise-Milestone, L.; Yee, A. J. M.; Wilson, B. C.; Whyne, C. M. The Benefits of Photodynamic Therapy on Vertebral Bone Are Maintained and Enhanced by Combination Treatment with Bisphosphonates and Radiation Therapy. *J. Orthop Res.* **2013**, *31*, 1398−1405.

(38) Alexenberg, C.; Afri, M.; Eliyahu, S.; Porat, H.; Ranz, A.; Frimer, A. A. Locating Intercalants within Lipid Bilayers Using Fluorescence Quenching by Bromophospholipids and Iodophospholipids. *Chem. Phys. Lipids* **2019**, *221*, 128−139.

(39) Man, D.; Slota, R.; Broda, M. A.; Mele, G.; Li, J. Metal-loporphyrin Intercalation in Liposome Membranes: Esr Study. *J. Biol. Inorg. Chem.* **2011**, *16*, 173−181.

(40) Chen, Y.; Gryshuk, A.; Achilefu, S.; Ohulchansky, T.; Potter, W.; Zhong, T.; Morgan, J.; Chance, B.; Prasad, P. N.; Henderson, B. W.; et al. A Novel Approach to a Bifunctional Photosensitizer for Tumor Imaging and Phototherapy. *Bioconjug Chem.* **2005**, *16*, 1264−1274.

(41) Harmatys, K. M.; Overchuk, M.; Chen, J.; Ding, L.; Chen, Y.; Pomper, M. G.; Zheng, G. Tuning Pharmacokinetics to Improve Tumor Accumulation of a Prostate-Specific Membrane Antigen-Targeted Phototheranostic Agent. *Bioconjug Chem.* **2018**, *29*, 3746−3756.

(42) Zheng, G.; Li, H.; Zhang, M.; Lund-Katz, S.; Chance, B.; Glickson, J. D. Low-Density Lipoprotein Reconstituted by Pyropheophorbide Cholesteryl Oleate as Target-Specific Photosensitizer. *Bioconjug Chem.* **2002**, *13*, 392−396.

(43) Kellgren, J. H.; Lawrence, J. S. Radiological Assessment of Osteo-Arthrosis. *Ann. Rheum Dis* **1957**, *16*, 494−502.

(44) Zhang, Y.; Vasheghani, F.; Li, Y. H.; Blati, M.; Simeone, K.; Fahmi, H.; Lussier, B.; Roughley, P.; Lagares, D.; Pelletier, J. P.; et al. Cartilage-Specific Deletion of Mtor Upregulates Autophagy and Protects Mice from Osteoarthritis. *Ann. Rheum Dis* **2015**, *74*, 1432−1440.

(45) Zimmermann, T.; Kunisch, E.; Pfeiffer, R.; Hirth, A.; Stahl, H. D.; Sack, U.; Laube, A.; Liesaus, E.; Roth, A.; Palombo-Kinne, E.; et al. Isolation and Characterization of Rheumatoid Arthritis Synovial Fibroblasts from Primary Culture–Primary Culture Cells Markedly Differ from Fourth-Passage Cells. *Arthritis Res.* **2001**, *3*, 72−76.

(46) Glasson, S. S.; Blanchet, T. J.; Morris, E. A. The Surgical Destabilization of the Medial Meniscus (Dmm) Model of Osteoarthritis in the 129/Svev Mouse. *Osteoarthr Cartil* **2007**, *15*, 1061−1069.

(47) Eckhard, U.; Huesgen, P. F.; Schilling, O.; Bellac, C. L.; Butler, G. S.; Cox, J. H.; Dufour, A.; Goebeler, V.; Kappelhoff, R.; Keller, U. A. D.; et al. Active Site Specificity Profiling of the Matrix Metalloproteinase Family: Proteomic Identification of 4300 Cleavage Sites by Nine Mmps Explored with Structural and Synthetic Peptide Cleavage Analyses. *Matrix Biol.* **2016**, *49*, 37−60.

(48) Bord, S.; Horner, A.; Hembry, R. M.; Compston, J. E. Stromelysin-1 (Mmp-3) and Stromelysin-2 (Mmp-10) Expression in Developing Human Bone: Potential Roles in Skeletal Development. *Bone* **1998**, *23*, 7−12.

(49) Krampert, M.; Bloch, W.; Sasaki, T.; Bugnon, P.; Rülicke, T.; Wolf, E.; Aumailley, M.; Parks, W. C.; Werner, S. Activities of the Matrix Metalloproteinase Stromelysin-2 (Mmp-10) in Matrix Degradation and Keratinocyte Organization in Wounded Skin. *Mol. Biol. Cell* **2004**, *15*, 5242−5254.

(50) Davidson, R. K.; Waters, J. G.; Kevorkian, L.; Darrah, C.; Cooper, A.; Donell, S. T.; Clark, I. M. Expression Profiling of Metalloproteinases and Their Inhibitors in Synovium and Cartilage. *Arthritis Res. Ther* **2006**, *8*, R124.

(51) Orbe, J.; Montero, I.; Rodríguez, J. A.; Beloqui, O.; Roncal, C.; Páramo, J. A. Independent Association of Matrix Metalloproteinase-10, Cardiovascular Risk Factors and Subclinical Atherosclerosis. *J. Thromb Haemost* **2007**, *5*, 91−97.

(52) Deraz, E. M.; Kudo, Y.; Yoshida, M.; Obayashi, M.; Tsunematsu, T.; Tani, H.; Siriwardena, S. B. S. M.; Kiekhaee, M. R.; Qi, G.; Iizuka, S. Mmp-10/Stromelysin-2 Promotes Invasion of Head and Neck Cancer. *PLoS One* **2011**, *6*, e25438.

(53) Zhang, G.; Miyake, M.; Lawton, A.; Goodison, S.; Rosser, C. J. Matrix Metalloproteinase-10 Promotes Tumor Progression through Regulation of Angiogenic and Apoptotic Pathways in Cervical Tumors. *BMC Cancer* **2014**, *14*, 310.

(54) Suzuki, K.; Morodomi, T.; Nagase, H.; Enghild, J. J.; Salvesen, G. Mechanisms of Activation of Tissue Procollagenase by Matrix Metalloproteinase 3 (Stromelysin). *Biochemistry* **1990**, *29*, 10261−10270.

(55) Heard, B. J.; Martin, L.; Rattner, J. B.; Frank, C. B.; Hart, D. A.; Krawetz, R. Matrix Metalloproteinase Protein Expression Profiles Cannot Distinguish between Normal and Early Osteoarthritic Synovial Fluid. *BMC Musculoskelet Disord* **2012**, *13*, 126.

(56) Blom, A. B.; Van Lent, P. L.; Libregts, S.; Holthuysen, A. E.; Van Der Kraan, P. M.; Van Rooijen, N.; Van Den Berg, W. B. Crucial Role of Macrophages in Matrix Metalloproteinase-Mediated Cartilage Destruction During Experimental Osteoarthritis: Involvement of Matrix Metalloproteinase 3. *Arthritis Rheum* **2007**, *56*, 147−157.

(57) Doan, T. N.; Bernard, F. C.; McKinney, J. M.; Dixon, J. B.; Willett, N. J. Endothelin-1 Inhibits Size Dependent Lymphatic Clearance of Peg-Based Conjugates after Intra-Articular Injection into the Rat Knee. *Acta Biomater* **2019**, *93*, 270−281.

(58) Chen, J.; Liu, T. W. B.; Lo, P.-C.; Wilson, B. C.; Zheng, G. Zipper" Molecular Beacons: A Generalized Strategy to Optimize the Performance of Activatable Protease Probes. *Bioconjug Chem.* **2009**, *20*, 1836−1842.